MODELLING THE ONSET OF FRICTIONAL SLIDING
Rupture fronts, slow slip, and time-dependent junction laws

by

JØRGEN KJOSHAGEN TRØMBORG

THESIS

for the degree of

Philosophiae Doctor

Prepared under joint supervision from the

Faculty of Mathematics and Natural Sciences
University of Oslo
and the
Laboratoire de Tribologie et Dynamique des Systèmes
École Centrale de Lyon

March 2015

Series of dissertations submitted to the
Faculty of Mathematics and Natural Sciences, University of Oslo
No. 1652

ISSN 1501-7710

Cover: Hanne Baadsgaard Utigard.
Printed in Norway: AIT Oslo AS.

Produced in co-operation with Akademika Publishing.
The thesis is produced by Akademika Publishing merely in connection with the thesis defence. Kindly direct all inquiries regarding the thesis to the copyright holder or the unit which grants the doctorate.

Contents

CHAPTER 1

Introduction

1.1 Motivation

Friction is scientifically interesting and technologically important. Friction is a collective term for the forces that resist relative motion of solid surfaces in contact, and it occurs wherever solid surfaces touch and can move against each other. The study of friction dates back thousands of years [34], but fundamental questions still remain unanswered.

Technologically, friction matters in every application that has moving parts, and in many applications that do not. First, friction can prevent motion, which can be either enabling or problematic depending on circumstances. Friction keeps objects in place, and without it, the slightest inclination of a surface would allow everything on it not locked in place by some other mechanism to slide off. When you put something down on the floor or a table, you can usually trust friction to keep it there. The flip side of this coin is that it makes heavy objects difficult to move, to the extent that the best solution is frequently to lift them out of contact instead of pushing them around.

Second, there is the direct energy loss. Friction opposes the motion of objects against each other, dissipating energy. This accounts for a significant part of the gross energy consumption of machinery. There is much to gain from reducing the energy lost to friction.

Third, the microscopic processes that lead to friction are also closely related to surface wear. The study of friction is therefore part of the wider field of tribology, which includes friction, lubrication and wear. The degradation of moving components is the most common reason that equipment stops working, from microelectromechanical systems to trucks.

Scientifically, friction is interesting because we do not yet understand it. We can often characterize it well, and I will summarize some theories of friction in Section 2.1, but to date, even the friction force between two macroscopic surfaces of known chemistry and topography under known external loading conditions can not be predicted from the bottom up. Instead, the friction must be measured in order to parametrize empirical descriptions. A major obstacle to predicting frictional properties is to link the behavior of the myriad microscopic connections that make up the overall interaction to the macroscopic behavior. As we shall see, part of the challenge is that describing the average behavior of the connections does not suffice; rather, the microscopic con-

nections influence each other directly or indirectly, and it is their collective behavior that must be scaled up.

The scope of this thesis is the onset of sliding in dry friction systems. I will not consider lubricated surfaces, nor will I consider wear.

The onset of sliding occurs through the breaking of the contacts that were keeping the interface stuck. Some recent experiments using fast cameras to monitor the breaking of the contacts in space and time have created new insights that start to fill in the knowledge gap between the microscopic and macroscopic scales. These experiments find that the interface does not break everywhere at the same time; instead, rupture nucleates at weak or highly stressed points and propagates outwards from there. The boundary between regions where the microscale junctions are broken and the interface is in a slipping state and the regions where the interface is still stuck is called the rupture front tip. The speed at which the rupture front tip travels as new junctions are broken is called the rupture front speed. Understanding the rupture fronts is a step towards understanding friction. The research presented here is aimed at answering some of the questions about rupture fronts that come out of the experiments.

1.2 Structure of the thesis

The thesis is organized as follows. Chapter 2 gives an overview of the scientific background for my research. Section 2.1 presents macroscopic friction laws and the underlying microscopic picture of multiasperity friction. Section 2.2 presents the experimental results that I have modelled, and Section 2.3 presents some of the questions raised by these experiments. Section 2.4 describes how other modelling groups have worked to understand the onset of sliding. Chapter 3 is a summary of the publications included in the thesis and their relationship to other results. Chapter 4 presents opportunities for future research.

There are four publications included in the thesis. The first and second have been published, the third is in review and the fourth is being prepared for submission. The publications appear in the format in which they are or will be published.

At the end of the thesis are three appendices. Appendix A discusses my choice of numerical integration scheme. Appendix B presents my verification of the bulk elastic solver through the simulation of simple shear and longitudinal waves. Appendix C presents two unpublished results related to Publications 1 and 3.

CHAPTER 2

Background

In this chapter I first give an overview of the theoretical and experimental background for my research. I then discuss the models that have been and are being used by others to study the onset of sliding. The scope of this chapter is not to review the field of friction, but to provide the context for my work and the details that are particularly useful background information for my publications.

2.1 Theory of friction

The friction between two bodies is fundamentally due to interactions occurring at their interface, on short length-scales. The results of these interactions, however, can also be observed and described on the length-scale of the bodies themselves. This leads to continuum laws for friction formulated as single-degree-of-freedom laws. In this section I summarize the most prominent single-degree-of-freedom friction laws. I also summarize the microscopic descriptions of multicontact interfaces.

2.1.1 Amontons–Coulomb friction

The most well-known of the single-degree-of-freedom friction laws are the so-called Amontons–Coulomb laws. They relate the friction force f on a sliding block sitting on a substrate (Figure 2.1) to the normal force F_N on the block as

$$f \leq \mu_s F_N \qquad , v = 0, \tag{2.1a}$$

$$f = -\text{sign}(v)\mu_d F_N \qquad , v \neq 0. \tag{2.1b}$$

Here v is the block's sliding speed, and $\mu_s \geq \mu_d$ are the static and dynamic coefficients of friction. The smaller-than-or-equal-to in the expression for static friction indicates that as long as the net external shearing force remains below the threshold $\mu_s F_N$, the block remains at rest. When the shear load reaches the threshold the block starts moving, and the friction force during sliding is dissipative, acting against the direction of sliding. Static friction is renewed immediately when the block comes to rest.

Although they are still useful as a first order description, the Amontons–Coulomb friction laws have been superseded by other single-degree-of-freedom friction laws. Still expressed in terms of a friction coefficient μ that multiplies the normal force, additional features of these friction laws include: (i) The transition from the static threshold to the

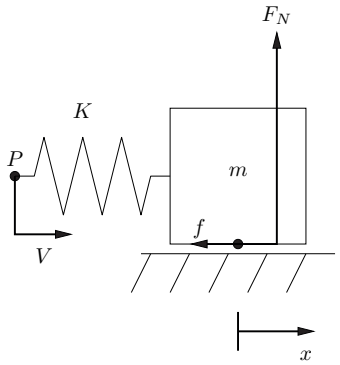

Figure 2.1: Sketch of a friction experiment. Shear and normal loads are applied and the dynamics of the block are observed. The position of the center of mass of the slider and the amplitudes of the external forces are examples of single-degree-of-freedom data that are usually collected. Here the spring with stiffness K represents the driving mechanism, P is a point on the driving mechanism that is being moved at speed V, m is the slider mass, F_N is the normal force on the slider from the substrate, and f is the friction force.

dynamic level is not infinitely sharp. Slip distance weakening and velocity weakening are the simplest model forms of regularization. (ii) The static friction level increases with increasing time spent at rest. This is called aging. (iii) The steady sliding dynamic friction level varies with the sliding speed v. Coulomb actually discovered (ii) and (iii) in 1821 [32], but only the form in Equations (2.1) became widely used, until the corrections were rediscovered in the mid-20th century. It is in honor of Coulomb's original work, perhaps, that some authors include small extensions of Equations (2.1) in the term Amontons–Coulomb friction, but for clarity I prefer to reserve this name for Equations (2.1) only.

In Section 2.1.2 I summarize the microscopic mechanisms that lead to the generality of the observation that friction force f is proportional to the normal force F_N. In Section 2.1.3 I introduce the rate-and-state friction framework, which incorporates the features (i)–(iii) and others that are not included in the Amontons–Coulomb friction laws.

2.1.2 Real contact area in multicontact interfaces

Equations (2.1), a good first approximation for many systems, asserts that friction is independent of the geometric (apparent) contact area between the slider and the substrate, and that friction is proportional to the normal load. Here I give the main points in the microscopic explanation of this result. I follow the review by Baumberger and Caroli [9].

That friction is proportional to the normal load and independent of the apparent contact area is not universally true. It is useful to distinguish interfaces between

- *rough hard solids*, for which loading levels that result in apparent pressures well below the elastic moduli do not give intimate molecular contact along the whole interface; and

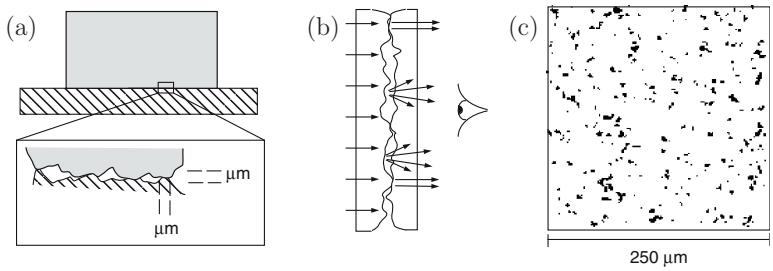

Figure 2.2: Direct measurement on transparent samples confirms that for multicontact interfaces the true area of contact (black spots) is much smaller than the apparent contact area (the full field of view). (a) Sketch of a friction experiments with the interface roughness highlighted. (b) Light is scattered at the rough non-contacting parts of the interface and transmitted at the real contacts. (c) After binarizing the image and inverting the colors the real surface area appears as black regions on a white background. Figure from Baumberger and Caroli [9] reprinted with permission from Taylor & Francis. Copyright © 2006 Taylor & Francis.

- *soft and/or smooth solids*, which get into real contact everywhere along their interface.

For soft or smooth solids, friction does depend on the apparent contact area, particularly for low normal loads where adhesion can dominate. Also, friction may or may not be proportional to the normal load, depending on the material. For rough hard solids, on the other hand, the apparent area independence and normal load proportionality result from robust geometrical mechanisms.

I will focus on rough hard solids, because the experiments I seek to model are of this type, as are most engineering materials. When an interface between rough hard solids is created by bringing the solids together, the highest points from each surface touch first. These contact points are called asperities. The resulting real contact area is smaller, often much smaller, than the apparent contact area (see Figure 2.2). The theory for the deformation of the asperities is different for plastic and elastic response, but the results are qualitatively the same.

It is found in contact mechanics [46] that the problem of two elastic spherical caps pressed together along their inter-center axis is equivalent to a single spherical cap (of a different radius and Young modulus) pressed against a rigid plane. This setup is called the Hertz contact, after Heinrich Hertz, who solved it first. In the Hertz contact, the real area A_{real} is not proportional to the normal load F_N, but grows as $F_N^{2/3}$. The Hertz solution holds within the linearly elastic regime, but breaks down when the material starts deforming plastically. The plastic deformation starts when the maximum stress, which occurs in the vicinity of the contact point, reaches the yield stress. The yield stress Y is a material property. If the normal force is increased further, the size of the plastified region increases. The contact is said to be fully plastic when the plastified region has volume $\sim a^3$, where a is the radius of the true contact.

Bowden and Tabor [16], working with metals, developed the microscopic explanation for friction in the case where the asperities that form where the rough hard surfaces touch are fully plastic. Their argument is as follows. First, they assume that the friction force a contact can resist is proportional to its contact area A_i, or equivalently that

the maximum shear stress σ_s a unit area can support is constant, $f_i = \sigma_s A_i$. Second, they assume that the net friction scales in the same way, $f = \sigma_s A_{\text{real}}$. (The $f \propto A_{\text{real}}$ scaling is found to hold, even though the net friction strength of the interface is generally smaller than the sum of the individual strengths because not all the contacts reach their maximum load simultaneously.) In the fully plastic contact the average normal stress $\bar{p}$ at the contact tip is approximately equal to the material hardness H, that is $\bar{p} \approx H$. (The hardness is related to the yield stress as $H \approx 3Y$.) Now, if all the microcontacts are in the fully plastic regime, $F_N = \bar{p} A_{\text{real}} \Rightarrow A_{\text{real}} = F_N/H \propto F_N$. It follows that $f = \mu F_N$, with $\mu = \sigma_s/H$.

The Bowden and Tabor picture explains the proportionality between normal load and friction force, through the proportionality between normal load and true contact area, but only in the fully plastic regime. It was some years before a similar result was developed for the regime where the contacts deform elastically. The Hertz result $A_{\text{real}} \propto F_N^{2/3}$ for a single contact was believed by many to remain true also in multicontact interfaces. It was Archard [2] who first came up with a multicontact model that predicts $A_{\text{real}} \propto F_N$. His idea was to use the Hertz result on an asperity covered in smaller asperities, themselves covered in smaller asperities, and so on. In other words, a fractal surface topography. He found that as the deformation of the large asperity increases, new contact points are formed as new microasperities come into contact, and this additional contribution to the real contact area brings the scaling up to $A_{\text{real}} \propto F_N$. He also performed experiments to support this, and he found that even when $A_{\text{real}} \propto F_N^n$, with $n < 1$, the friction force was proportional to A_{real}, this relationship being more fundamental than the relationship between friction and normal load.

About a decade after Archard's publication of [2], Greenwood and Williamson [43] came up with a simpler surface topography model yielding $A_{\text{real}} \propto F_N$, and they performed experiments to measure the parameters in their model. The Greenwood–Williamson model approximates the surface topography as a set of spherical caps of equal radius, but with a non-constant distribution of heights. The idea behind this approximation is sketched in Figure 2.3. Treating each sphere as a Hertzian contact and using the separation d between the average surface planes as an independent variable, they calculated that for an exponential distribution of heights, the normal load and the true area have the same scaling with d, thus $A_{\text{real}} \propto F_N$. They measured the surface height distributions of many samples and found that they were well fit by Gaussians. The highest contacts are in the tail of the distribution, and those contacts form first. Because the tail of the Gaussian distribution and the exponential distribution are sufficiently similar, the proportionality between normal load and true area still holds for their samples, even though it is exact only for the exponential height distribution. They further defined a plasticity index that can be used to determine whether, under reasonable normal loads, a surface will be in the elastic or the plastic regime.

The key points from this section are: (i) The proportionality between normal load and true contact area. This result is found to be very robust, which gives validity to the concept of a friction coefficient $\mu = f/F_N$; this concept will be refined in the next section. (ii) The multiasperity picture of the frictional interface, which I have pursued in my research.

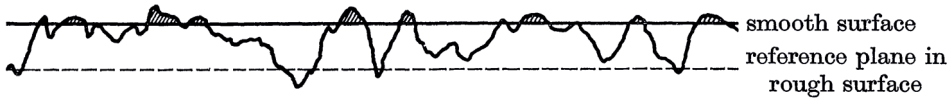

Figure 2.3: The idea behind the Greenwood-Williamson model of contact between rough surfaces. The load is supported by the asperities (shaded) having heights greater than the separation between the reference planes. The model approximates these asperities as Hertzian spheres of equal radius, but with a random variation of heights above the reference plane in the rough surface. Figure from Greenwood and Williamson [43] reproduced with permission from JSTOR. Copyright © 1966, The Royal Society.

2.1.3 Rate-and-state theory

Rate-and-state theory seeks to incorporate into the continuum description of friction, in a few equations, some of the most important features that are neglected by the Amontons–Coulomb friction laws. These are: (i) the increasing static friction with increasing time in stationary contact; (ii) the velocity dependence of steady-state sliding friction; (iii) the direct effect, which will be described below. The *rate* variable is the sliding velocity of the center of mass, $\dot{x}_{CM}$. The *state* variable is often linked to the time spent in contact or the growth of the real contact area, but does not always have any direct physical interpretation ([9]).

James H Dieterich [37, 38] made important experimental work on rock samples that lead to the development of rate-and-state theory. He also contributed to the theory [36]. Important additions to the theory were made by Andy L Ruina and James R Rice [70, 78]. I have based the presentation here on the reviews of Baumberger and Caroli [9] and Marone [56].

Figure 2.4 shows experimental evidence of aging. Figure 2.4a is data from [37] and shows the measured macroscopic static friction coefficient (the peak in the ratio of the imposed shear and normal forces) in slide-hold-slide experiments as a function of the hold time. Figure 2.4b and c shows the growth in the true area of contact with hold time. The growth in the true area is the favoured explanation for the growth in the macroscopic static friction.

Figure 2.5 shows the velocity dependence of steady state sliding, and the direct effect.

In 1983 Ruina [78] published a thorough examination of rate-and-state variable friction laws. The theory he presents is a framework into which many specific rate-and-state friction laws can be cast. In its most general form presented below, rate-and-state theory includes a very wide range of formulations.

The basic assumption is that the surface (or surface region) has, at any instant in time, a state. Also, the friction stress τ depends only on the slip rate v, the normal stress σ and the state $\boldsymbol{\theta} = \theta_1, \theta_2, \dots$. That is,

$$\tau = \sigma F(v, \theta_1, \theta_2, \dots), \tag{2.2a}$$

where F is some function. The rate of change of the state is assumed to depend only on the state itself, the slip rate and the normal stress,

$$\mathrm{d}\theta_i/\mathrm{d}t = G_i(\sigma, v, \theta_1, \theta_2, \dots). \tag{2.2b}$$

To make this more explicit, Ruina gives a handful of examples of laws that fit this form.

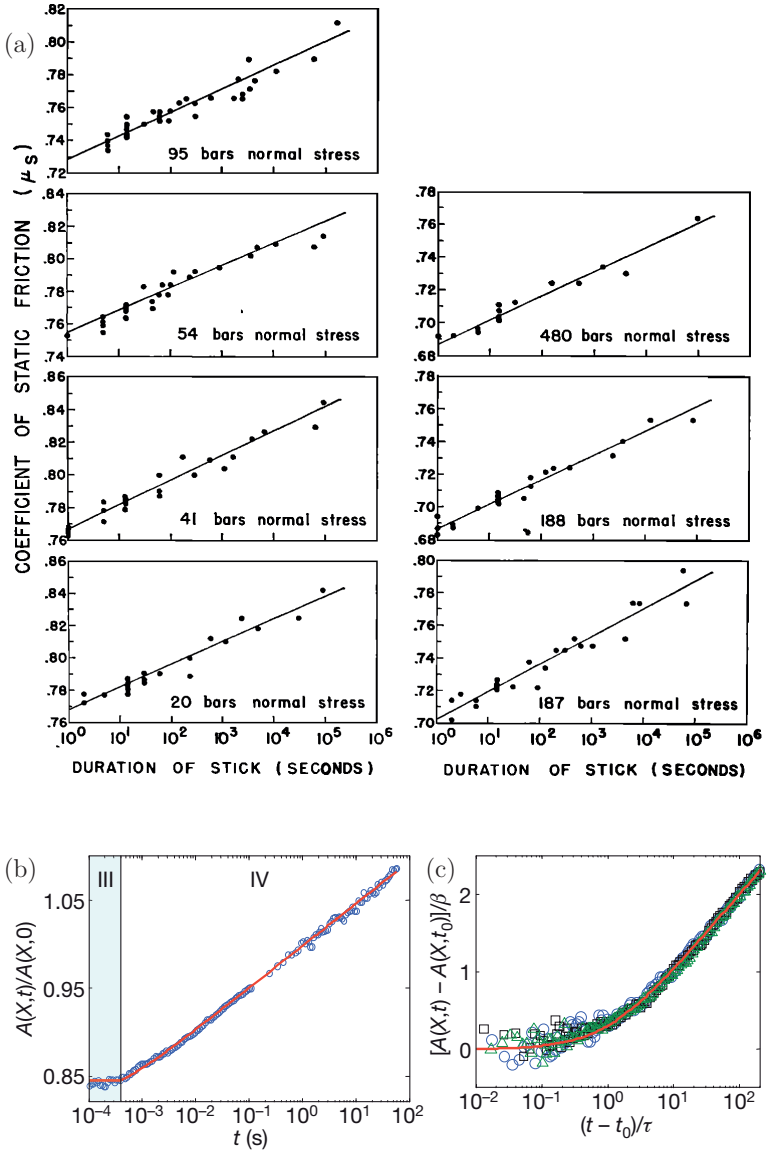

Figure 2.4: (a) Macroscopic static friction coefficient measured in slide-hold-slide experiments on sandstone. The static friction increases logarithmically with hold time. (b, c) Evolution of the true area of contact measured in poly(methyl methacrylate). (b) The boundary between regions III and IV mark the cessation of slip. The data is normalized against its own value at time $t = 0$ (at which the onset of slip occurred). (c) Data from three different experiments all fit the equation $A_{\text{real}}(t) = A_{\text{real}}(t_0)[1 + \beta \log(1+(t-t_0)/\tau)]$, where t_0 is the time of slip arrest and β and τ are fitting parameters. Figure (a) from Dieterich [37] reproduced with the permission of John Wiley and Sons. Copyright © 1972 by the American Geophysical Union. Panels (b, c) from Ben-David et al. [12] reprinted by permission from Macmillan Publishers Ltd: Nature, copyright © 2010.

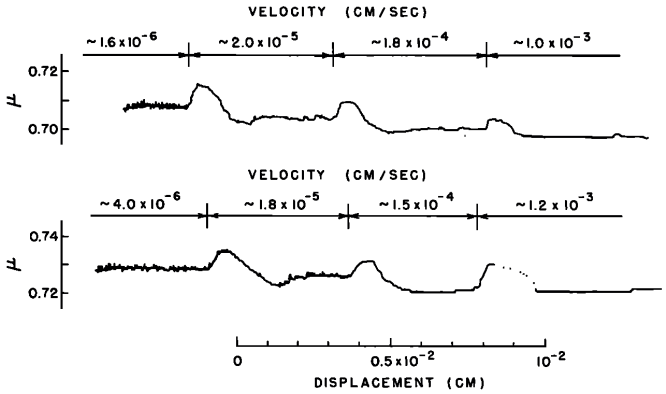

Figure 2.5: Experimental results showing velocity dependence of steady state sliding, and the direct effect. The driving velocity for each part of the curves, delimited by the horizontal bars, are different. The velocity dependence of steady state sliding friction is seen in the difference in the levels to which μ converges. The direct effect is the transient increase in μ with increasing driving velocity and accompanying decay to the steady state value. The decay occurs over a characteristic length D_0 that Dieterich [38] writes "appears to be independent of the magnitude in the change of velocity but does correlate with surface roughness". The sample is granodiorite rock. Figure from Dieterich [38] reproduced with the permission of John Wiley and Sons. Published in 1979 by the American Geophysical Union.

Although very general in principle, in practice, the term rate-and-state constitutive law is frequently associated only with one or two of the most widely used examples of such laws. Marone [56] reviews the differences between these. In modern notation the law proposed by Dieterich is

$$\mu\left(\dot{x}_{CM}, \vartheta\right) = \mu_0 + \mathfrak{a} \ln\left(\frac{\dot{x}_{CM}}{V_0}\right) + \mathfrak{b}\left(\frac{V_0 \vartheta}{D_0}\right), \tag{2.3a}$$

$$\dot{\vartheta} = 1 - \left(\frac{\dot{x}_{CM}\vartheta}{D_0}\right). \tag{2.3b}$$

Note that for $\dot{x}_{CM} = 0$, $\vartheta = t$, which justifies interpretation of this state variable as a "time-like" variable. The empirical coefficients $\mathfrak{a}$ and $\mathfrak{b}$ are positive and of order 10^{-2}. V_0 is a reference velocity in the range (0.1–100 μm/s).

In his analysis of Dieterich's and other forms of the evolution of the state variable ϑ, Ruina [78] proposed replacing Equation (2.3b), with

$$\dot{\vartheta} = -\frac{\dot{x}_{CM}\vartheta}{D_0} \ln\left(\frac{\dot{x}_{CM}\vartheta}{D_0}\right). \tag{2.4}$$

Microscopically, the two forms have a different interpretation: Dieterich's form emphasises the average contact lifetime, while in Ruina's form, any change in friction requires slip. However, distinguishing between the laws in the laboratory has proven difficult [56]. According to Scholz [79], the rate-and-state relationship in best agreement with experimental observations is equations (2.3), which is somewhat ambiguously called the Dieterich–Ruina law.

The problematic property of the logarithms in equation (2.3a) and equation (2.4) that they diverge to negative infinity when their arguments approach zero is remedied by adding a +1 term, so that for example $a \ln\left(\frac{\dot{x}_{CM}}{V_0}\right) \to a \ln\left(1 + \frac{\dot{x}_{CM}}{V_0}\right)$. This solution is used by [5, 6, 15], whose application of rate-and-state friction to the study of rupture front propagation I summarize in Section 2.4.3, and in the fitting equation for Figure 2.4b.

2.2 Experimental results that call for new modelling efforts

To recap the background up to this point in the text: We have empirical single-degree-of-freedom friction laws that when parametrized correctly successfully account for the observed single-degree-of-freedom dynamics of many frictional systems. We also have microscopic theories that explain the features observed on the macroscale. However, the link between the scales is missing. By this I mean that we are missing a theory that takes as its starting point loading conditions and the chemistry and topography of the opposing interfaces, and from this information predicts the friction dynamics.

One of the difficulties in building a bottom-up friction theory is that large and small scale evolutions both influence each other strongly. The load on each microscopic junction is the result of how the external load is transferred through the bulk of the material to the frictional interface. The change in the external load in turn depends on the motion of the sliding system, which depends on the evolution of the junctions (the slider can only move by breaking the junctions that are keeping it in place). This two-way coupling makes it difficult to scale up from the microscale to the macroscale.

Experiments can help bridge the gap between the micro- and macroscales by measuring directly what takes place at intermediate scales. Such experiments acknowledge that frictional objects are not rigid, but have some non-zero compliance. In other words, the objects deform. Therefore, the interface does not usually start sliding at the same time everywhere; the frictional contacts do not all break simultaneously. By measuring in detail how the transition from the stuck to the sliding interface occurs, the experiments can provide information on the links between the micro- and macroscales.

There are many experiments that investigate the onset of sliding by measuring where rupture starts and how it propagates. Quasistatic rupture, where the growth of the slipping region is proportional to the external loading rate, was studied in e.g. [30, 67]. Dynamic rupture fronts were studied in e.g. [3, 23, 58, 74, 77]. Dynamic rupture propagating at speeds higher than the shear wave speed (supershear rupture) is the topic of e.g. [58, 73, 73, 83]. Many more could be named. However, I will not attempt to review the experimental literature here. Instead, I spend most of this section on the experiments by Fineberg's group, because their results have been the direct inspiration of my own research.

2.2.1 Fineberg group

By definition, the frictional interface is situated between two pieces of solid material. Placing mechanical sensors within the interface bears the double difficulty of doing this without modifying the intrinsic dynamics and this being a harsh environment for the sensors. One solution to this experimental challenge is to use transparent samples

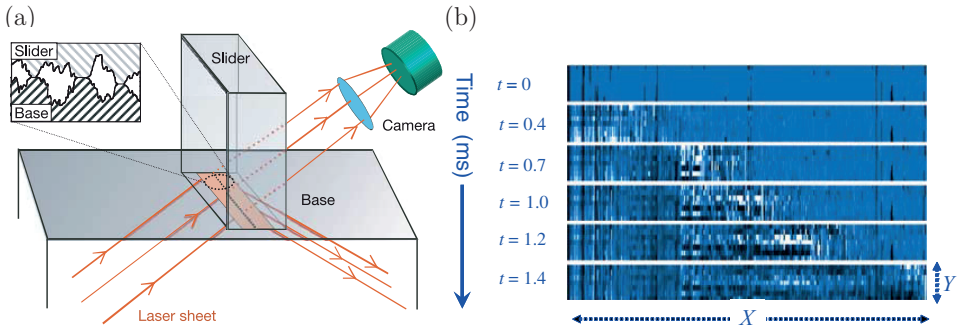

Figure 2.6: (a) Sketch of an experimental technique for accessing interface information directly. (b) Frames from a video of a rupture event. Each frame shows the full interface. Local changes in figure color between two frames indicate breaking and reformation of the contacts within that pixel. The light intensity received at the camera is proportional to the true area of contact. Panel (a) from Rubinstein et al. [74] reprinted by permission from Macmillan Publishers Ltd: Nature, copyright © 2004. Panel (b) from Rubinstein et al. [77] copyright © IOP Publishing. Reproduced by permission of IOP Publishing. All rights reserved.

and capture a high frame rate video of the interface. The experimental protocol of the Fineberg group is described in some detail in [75]. In short, the interface between two blocks of poly(methyl methacrylate) (PMMA) is illuminated with a laser sheet. The surfaces of the PMMA blocks have been first smoothed to optical flatness and then roughened with abrasive paper to create an extended rough interface. Illuminating this interface with a laser sheet at a shallow angle results in total internal reflection in the areas that are out of contact, and transmission only at the points of real contact. Imaging the transmitted light with a fast camera taking on the order of tens of thousands of images per second produces a video where contact breaking and renewal is seen as changes in the intensity level. Each pixel averages over an area of 0.1×1.5 mm^2, estimated to include ~ 1500 contact points.

Figure 2.6 shows a sketch from one of the experimental papers ([74]) and 6 selected frames from one of the videos ([77]). Each frame is a picture of the whole frictional interface. Where the pixel color changes from one frame to the next, the contacts within that pixel have been broken and/or reformed. Comparing the second frame to the first you see that the leftmost quarter of the interface has started slipping (contacts have been renewed) while the rest of the interface is still intact. The boundary between the slipping and stuck regions advances in these frames to ca. 2/5 in the third frame, then 2/4, 3/4 and finally to the leading edge in the last frame. Events like this one, which reaches the leading edge, are called full sliding events. Sometimes the events arrest before reaching the leading edge; these are called partial slip events. Partial slip events that occur before the first full sliding events are called precursors.

The sliders used in these experiments are 140 or 200 mm long, 75 mm high, and 6 mm wide. This makes the measurement along the frictional interface relatively one-dimensional, as can also be seen in Figure 2.6b: the front reaches a given distance x from the trailing edge at the same time for all values of y. By averaging over the y-values, a single row of data for each point in time is obtained. Figure 2.7a shows

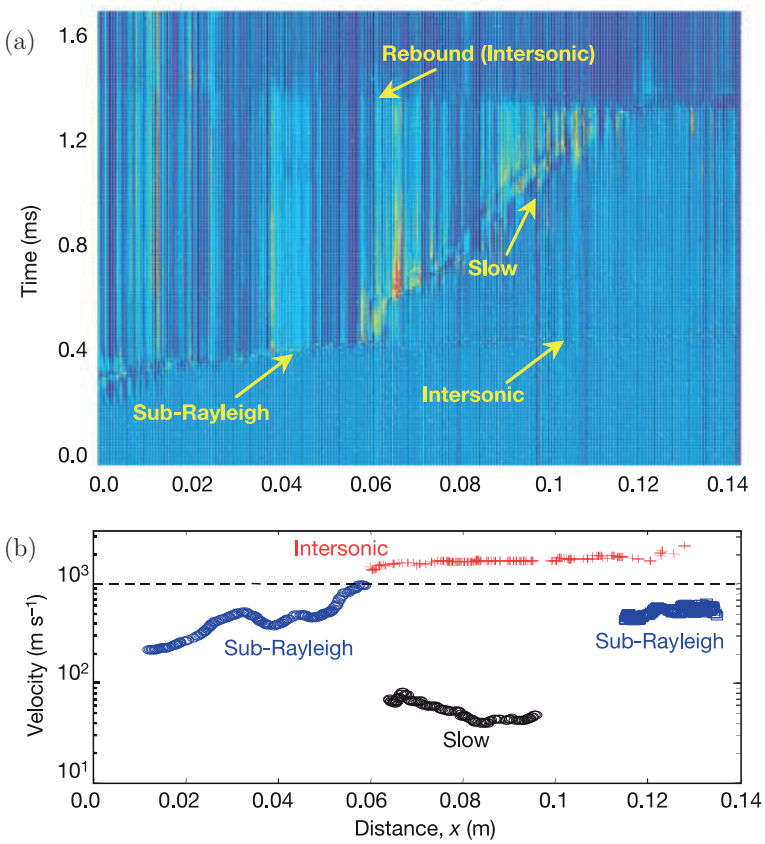

Figure 2.7: (a) Spatio-temporal evolution of a rupture event. Each row shows one snapshot in time of the whole interface. That is, each frame in data like Figure 2.6b, averaged over the short dimension, becomes one row in this figure. Each column shows the evolution in time at one location along the interface. Sharp contrast indicates breaking and reformation of most of the microscopic junctions. The rupture front line is indicated by text and arrows. (b) The (inverse) slope of the rupture front line in (a) gives the front velocity as a function of position. Figure from Rubinstein et al. [74] reprinted by permission from Macmillan Publishers Ltd: Nature, copyright © 2004.

these individual time rows stacked vertically to create a spatiotemporal plot of the propagation of the rupture front. Each column in Figure 2.7a shows the evolution in time at one location along the interface. The propagation of the rupture front can be seen from the image contrast associated with the breaking and reformation of junctions. The rupture front speed is the (inverse) slope of the rupture front line and is shown in Figure 2.7b. One of the intriguing aspects of Figure 2.7 is how the main rupture front starts its propagation at the fast, sub-Rayleigh speed, then transitions to much slower propagation, and then transitions back to fast propagation.

The propagation speed of the point separating the already slipping and the still stuck regions, the rupture front tip, is interdependent with the speed at which material in the sliding objects move. I use the names rupture front speed and material slip

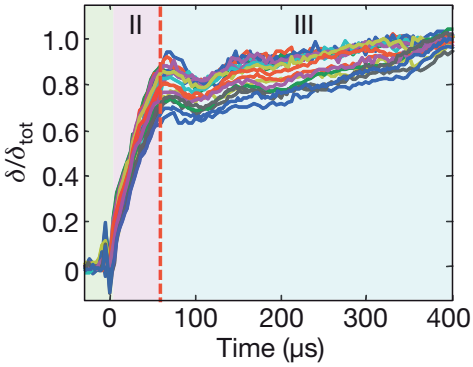

Figure 2.8: The material slip vs time, measured approximately 25 mm from the trailing edge of a 200 mm long sample in precursor events. Note in particular the transition from a high slope (fast slip) to a lower slope at a common time marked by the red dashed line (60 μs). δ_{tot} is the total slip in each event, and ranges from 4 μm to 20 μm. The time scale which emerges from this figure is distinct from the classical aging time scale, also measured in this experiment, and motivates our choice to study friction laws were junction renewal is time-controlled. Figure from Ben-David et al. [12] reprinted by permission from Macmillan Publishers Ltd: Nature, copyright © 2010.

speed, or the short-hand versions front speed and slip speed. The front speed depends on the slip speed behind the front tip, because it is the deformation of the sliding objects that bring energy to the front tip. The slip speed in turn depends on the front speed; for example, without rupture there is no slip (neglecting creeping motion where contacts under load fail gradually or individually over time).

From tracking markers or a set of gridlines, the material slip can be measured. Figure 2.8 shows the resulting profiles $\delta(t)$ from Ben-David et al. [12]. A very interesting observation to be made from this data is the data-collapse that is obtained when rescaling with the total slip δ_{tot}. The fact that no rescaling along the time axis is required indicates that a common time scale exists between these events. This time scale controls the fast dynamics with which the interface arrests after slipping. It is therefore distinct from the classical time scale for aging, also observed in [12] (see Figure 2.4), which controls the slow strength recovery of the interface when it is at rest. This is an important motivation for our choice to study friction laws where junction renewal is time-controlled.

The main topic of Publications 1, 3 and 4 are the speed of rupture fronts, the transitions in front speed within rupture events and the link between slip speed and front speed. Ben-David et al. [11] showed that one of the measures that strongly influence the front speed is the local ratio of shear to normal stress $\tau(x)/p(x)$ just before the event starts. I include their data in Figure 2.9. The $\tau(x)/p(x)$ dependence gives 2D models an important advantage over 1D models. In 2D, the normal stress field $p(x)$ can evolve according to the deformation of the slider rather than being prescribed (it can also be prescribed when this is desirable), and the application of external loading conditions that mimic the experimental conditions create a shear stress field $\tau(x)$ that is a closer approximation to the experimental result than 1D models do.

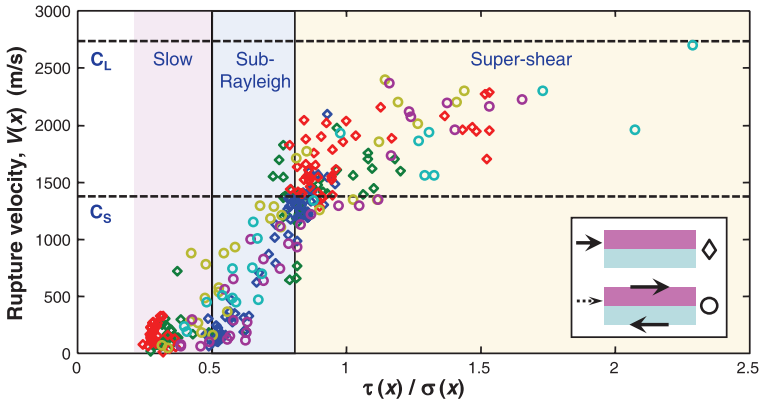

Figure 2.9: The local rupture front speed depends strongly on the local shear to normal stress ratio just before the front starts. The scatter indicates that other parameters are also important. We propose some explanations in Publication 3. Each data point is measured away from the slider edges, in system-sized sliding events. The marker colors indicate the location of the sensors and the marker shape indicates the shear loading conditions (edge-loading or predominantly uniform loading as shown in the legend). Figure from Ben-David et al. [11]. Reprinted with permission from AAAS.

2.2.2 Baumberger et al.

I have presented the Fineberg group's experiments first in this section for clarity of presentation, and because they are the most direct inspiration of my own research. The observation of rupture fronts in friction is not limited to the Fineberg group, however, as should also be clear from the introduction to this section. Already in 2002, Baumberger et al. [10] studied the onset of sliding in a gel–glass interface. They too filmed the frictional interface, and due to imperfections at the gel surface they were able to monitor the position of each part of the interface in time. They found that when slip nucleates, in their case near the trailing edge, a rupture front (they call it a slip pulse) travels towards the leading edge. The material behind the front tip is slipping, while the material ahead of the front tip remains stuck. Figure 2.10 shows a spatiotemporal map of sliding onset. This figure is conceptually very interesting in that it exhibits *both* the material slip speed and the rupture front speed.

2.2.3 Nakano et al.

Maegawa et al. [55] performed both experiments and simulations to study the precursors to sliding in a PMMA-on-PMMA experiment. The main new feature compared to the Fineberg group's experiments is the application of a strongly varying normal force profile along the slider. This modifies the triggering and arrest of precursor events, leading to changes both in the shape of the curve relating precursor length to driving force, and in the number of precursors. This work helped highlight that precursors are strongly linked to the shape of the shear and normal stress fields. This is illustrated in Figure 2.11.

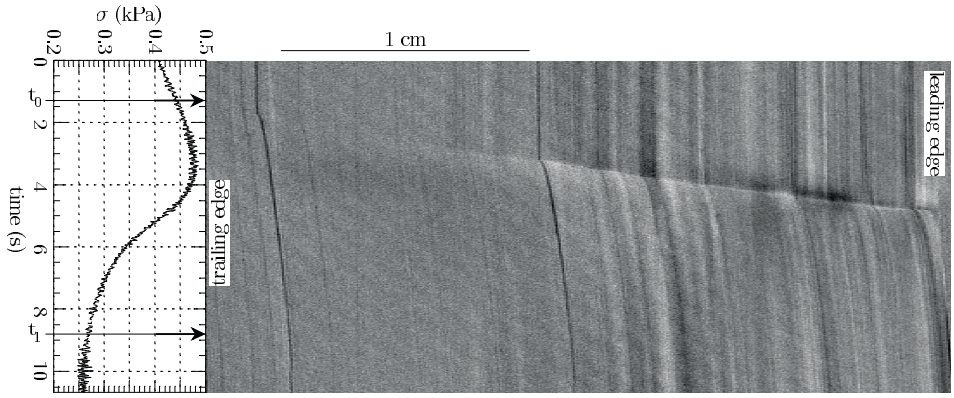

Figure 2.10: Experimental observation of the onset of sliding at a gel–glass interface. Each row in the grey image corresponds to a line of pixels registered in a camera filming the interface, parallel to the loading direction. The greyscale variations are due to imperfections at the gel surface, and allow tracking the motion of the gel. Time increases downwards. The local slip speed can be determined from the positions of the imperfections. The onset of local slip appears as a slope discontinuity. The boundary between slipping and stuck regions travels from the left at t_0 and reaches the leading edge $t \approx 5\,\mathrm{s}$. The slope of this boundary is the rupture front speed. This figure is conceptually very interesting in that it exhibits both the material slip speed and the rupture front speed; the relationship between these will be one of the important results in Publications 1 and 3, albeit in a different material. On the left of the figure is the loading curve, that is the time evolution of the driving force F, expressed as the average shear stress $\sigma = F/A$, where A is the apparent contact area. Figure from Baumberger et al. [10] reprinted with permission from APS. Copyright 2002 by the American Physical Society.

2.3 Outstanding questions

The experiments described in the previous section have provided new insights into the onset of frictional sliding. They have also raised new questions, many of which center on the properties of the rupture fronts. Some outstanding questions are:

(a) What determines the propagation speed of a rupture front?

(b) Are there distinct mechanisms behind the different front types (fast/slow), or are the fronts fundamentally the same?

(c) What determines the transitions between fast and slow front propagation?

(d) To what extent do the fronts determine the macroscopic static friction? Do the fronts affect the dynamic friction?

(e) How would the fronts propagate if the frictional interface was more quadratic in shape, rather than a thin strip?

(f) Can we understand the nucleation of fronts, their arrest, and how arrest and nucleation influence each other?

(g) How can we upscale from the microscopic pictures of Section 2.1.2 to the mesoscale and macroscale behavior?

(h) What can we learn of fronts in other frictional systems, like earthquake faults, from these laboratory experiments?

How others have addressed these questions will be the topic of Section 2.4. How we have addressed them is the topic of the publications. We provide answers to (a), (b) and (c). We also bring new insights into (f) and (g), and to lesser extent (d) and (h). Question (e) is not addressed here.

2.4 Models of extended frictional interfaces and of rupture fronts

It is useful to consider a friction simulation to be the combination of a friction law, a law for the deformation of the bulk material, and the external loading conditions. There is a range of possible choices for each component. The simplest bulk model is the point system, that is, a single, rigid block sliding on a substrate that interacts frictionally with the block, but does not itself move or evolve. The point system is the level at which the interface friction laws are usually formulated. The Amontons–Coulomb and the rate-and-state laws describe point systems. Simulating the point system is a good tool for investigating the properties of a friction law. However, there can be no partial rupture and no rupture fronts in the point system, because the whole slider is a rigid unit. To resolve the transition to sliding in space and time requires at least a one-dimensional model. Perhaps the simplest such model is the 1D spring–block model. In this model, the total mass of the slider is distributed among a linear chain of blocks, themselves point systems, that interact with their neighbors. Spring-and-dashpot interactions are common.

In this section I will give an overview of the models of extended frictional interfaces and of rupture fronts that have been central to the research presented in this thesis. Some of these models have directly inspired our own models, for example those by Braun and Peyrard [17], Braun et al. [22], Maegawa et al. [55], Persson [64]. Other models presented here have been developed and investigated during the time I did the thesis research, influencing our thinking without being incorporated in our work explicitly.

Most of the publications on which I base this overview have multiple authors, and usually there are a handful of publications on each model by roughly the same group of authors. There is also collaboration between the different groups of authors. The dividing lines I make in the text to create structure and identify distinct modelling approaches are of my own devising; other delineations may be preferred by others.

2.4.1 Nakano, Matsukawa and co-workers

The first friction simulations I was part of were of the 1D spring–block model with Amontons–Coulomb friction applied at each of the small blocks. This was directly inspired by a publication by Maegawa et al. [55], itself part of a tradition that goes back to a combined simulation and analog model by Burridge and Knopoff [24]. This numerical model combines a simple and successful friction law for a point system with a simple law for the deformation of the bulk material.

The experiments by Maegawa et al. [55] were very briefly discussed in Section 2.2.3. In their numerical simulations, they applied a 1D chain of ten blocks connected by springs, each block interacting with the substrate through simple Amontons–Coulomb friction. By applying the shear load from the trailing edge they produced a series of precursors and compared them to their experimental results. They found similar trends upon changes to the normal load asymmetry. I return briefly to this model in Section 2.4.2.

Otsuki and Matsukawa [62] performed finite element simulations and analytical calculations on a model with a velocity weakening extension of the simple Amontons–Coulomb friction law. In this model, the transition from static to dynamic friction upon rupture is not instantaneous, but instead occurs linearly over a characteristic slip speed range. They study the precursors to sliding. They find that because of the precursors, the macroscopic static friction is lower than the local static friction, and further that the magnitude of this reduction depends on the system length and the external normal load. For longer systems and higher normal loads, the macroscopic static friction, i.e. the ratio of the shear force required to make the system slide to the normal force, decreases. A normal load dependence similar to their theory is observed in their experiments reported in [50]. Fig. 3 in [55] (the same experimental system) indicates that the real area *is* proportional to the normal load. Together, these observations imply that the macroscopic static friction in the experiment is not proportional to the real area. This makes their result contrast with those of Archard [2] discussed in Section 2.1.2, who found that the friction was proportional to the real area even when the real area was not proportional to the normal load.

2.4.2 Our own work prior to my PhD

Our findings from working on and extending the 1D spring–block model of Maegawa et al. [55] with Amontons–Coulomb friction are reported in Amundsen et al. [1] and in Publication 4. One of the disadvantages of using simple Amontons–Coulomb friction in a 1D model of an extended interface is that the model does not reproduce the shear stress fields in the experiments well. Each block is stationary until the load on it reaches the static friction threshold, and under side loading conditions the load is only transferred into the sample when blocks slip. Because of this, the external load acts only on the single block it couples to directly. In contrast, in experiments, there is some physical length scale over which the external load is distributed.

The distribution of the external load over a physical length can be achieved by changing the friction law, the bulk law or the external loading conditions. The end-member cases of external loading are point loading, usually on either end of the chain of blocks, and uniform loading of every block. We have used the terms side loading and top loading (because a near-uniform load is often achieved experimentally by attaching the top of the slider to a rigid object and imposing the external load on this object instead of on the slider directly). In simulations, loading schemes that introduce a physical length by coupling the external driving to a subset of blocks and with individual coupling strengths can be defined, but I have not seen this done, perhaps because no clear experimental analogue can be found in use. The introduction of a physical length through the friction law or the bulk law, however, has been used both by us and others.

In Amundsen et al. [1] we introduced a modified Amontons–Coulomb friction law where each block couples to the substrate through a spring modelling the shear compli-

ance of the microcontacts. The spring breaks at the static friction threshold force, and the dynamic friction during sliding is unmodified. The essential difference introduced by the spring is that while stuck, a block can accommodate a small motion which distributes some of the load on it onto its next-in-line neighbor, which in turn moves a short distance and distributes some load further down the chain, and so on. The ratio of the inter-block to the block–substrate stiffnesses controls the physical length scale over which the stress field set up by the external load extends. This remedies the very strong resolution dependence the side-driven 1D model has when there is no interfacial compliance.

The variation in normal force/stress at the interface and the coupling of normal and shear stress through Poisson expansion are not naturally part of a one-dimensional model, but can be included by specifying them by hand. They arise spontaneously, however, if the vertical (out of the friction plane) dimension is included in the simulations. In Trømborg et al. [81] we combined the rigid Amontons–Coulomb friction law with a 2D spring–block model. The physical length scale over which the external load acts scales with the height at which it is applied.

It can be useful to distinguish between the static and dynamic elements of the onset of sliding. I will call static those measurements that are taken when the material is at rest. Examples are the shear and normal stress fields just before rupture nucleation, and the length of precursors. I will call dynamic those measurements that are taken while the material and/or the rupture front are in motion. The slip and front speeds are examples of dynamic measurements. In this thesis I am mainly concerned with the dynamic measurements. However, our first demonstration of the benefit of a 2D simulation over a 1D simulation was in the study of static measurements in our earlier publication Trømborg et al. [81]. I will quickly review the main results in Figures 2.11 and 2.12.

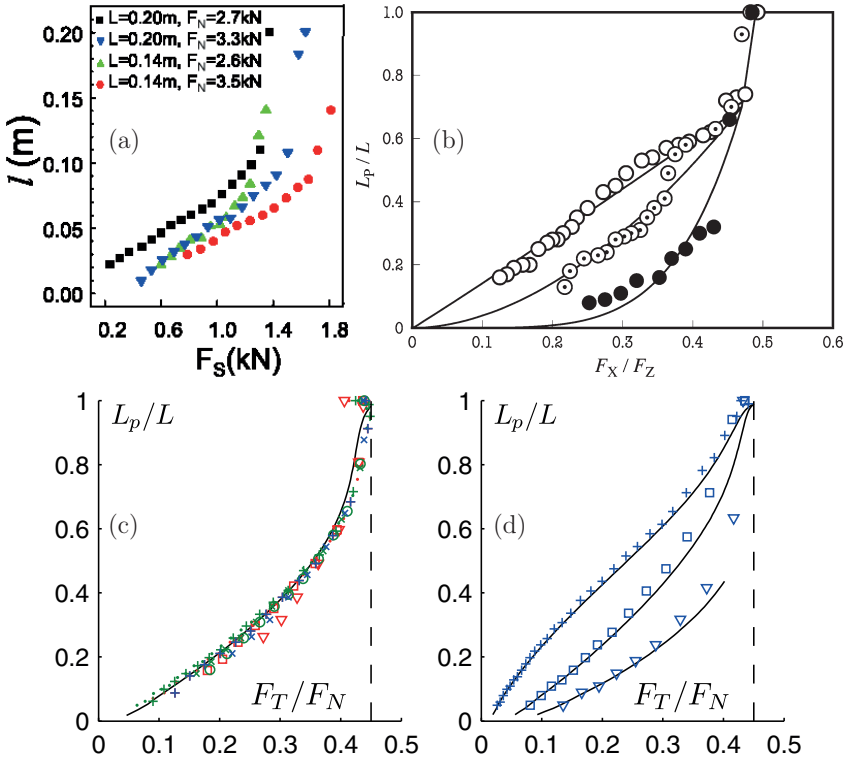

Figure 2.11: The length of precursors as a function of the driving force at which they occurred. Our simulations (c, d) agree well with experiments (a, b). In (a) the different lines correspond to different sample sizes and normal loads, and can be collapsed by rescaling with these parameters. In (b) the different lines correspond to different normal load asymmetries, and highlight that the precursors are strongly linked to the shape of the shear and normal stress fields. In (c, d) we mimicked the experimental loading conditions and reproduced the shape of the lines as well as the number of precursors better than 1D models had been able to do. Panel (a) from Rubinstein et al. [76] reprinted with permission from APS. Copyright 2007 by the American Physical Society. Panel (b) from Maegawa et al. [55] reproduced with kind permission from Springer Science and Business Media. © Springer Science+Business Media, LLC 2010. Panels (c, d) are from Trømborg et al. [81].

The original caption for panel (b) is reproduced here as required by Springer: Relationship between the propagation length L_p of precursors and the tangential load F_X under different loading conditions. L: length of the longitudinal line contact (= 100 mm); *dotted circle*: uniform loading ($F_{ZA} = F_{ZB} =$ 200 N); *solid circle*: non-uniform loading ($F_{ZA} = 300$ N and $F_{ZB} = 100$ N); and *open circle*: non-uniform loading ($F_{ZA} = 100$ N and $F_{ZB} = 300$ N).

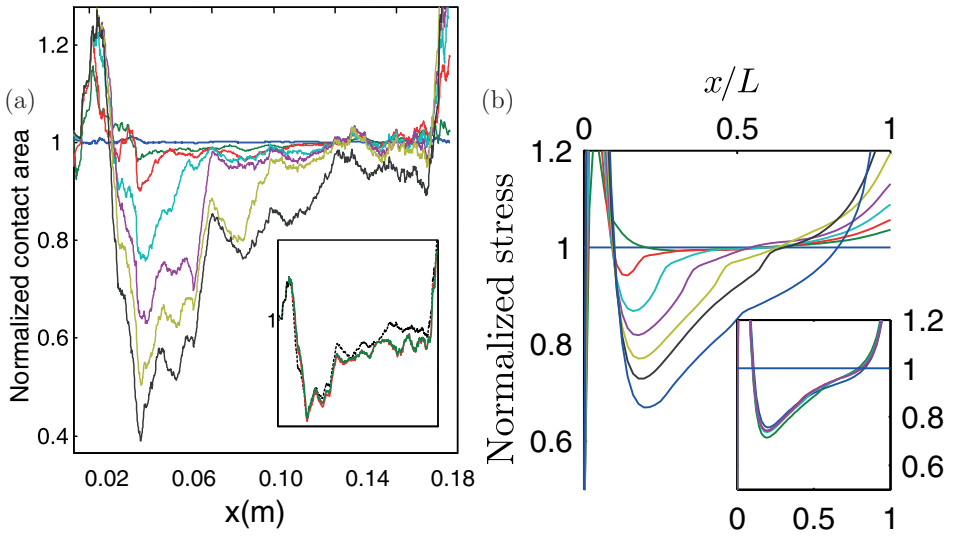

Figure 2.12: The change in local area as the precursors invade the interface as observed in experiments (a) can be explained from changes in the normal stress profile as measured in 2D simulations (b). Each precursor shown propagates farther than the preceding one, and modifies the local area and the normal stress over a successively larger part of the interface. The insets show the local area and the normal stress profile after full sliding events. They remain the same between events. This was deemed surprising in the experimental paper, but fits well with our finding that the spatial redistribution of the true area corresponds to a spatial redistribution of the normal load. Panel (a) from Rubinstein et al. [76] reprinted with permission from APS. Copyright 2007 by the American Physical Society. Panel (b) is from Trømborg et al. [81].

2.4.3 Bouchbinder group (rate-and-state)

The model studied by Bouchbinder and co-workers in [5, 6, 15] is a rate-and-state formulation of the interaction between the slider and the interface. This is applied at the level of individual blocks (mass units in the discretization) in a 1D model. The authors also perform analytical calculations in a "quasi-1D" model in which they report 1D solutions that depend on a length scale H that represents the height of the slider, assumed to be small compared to the length scale over which the fields vary along the interface.

Their friction law, being a rate-and-state law, encodes the evolution of a frictional stress τ, which depends on a state variable ϕ, and the evolution of ϕ itself. Both evolution equations involve the slip velocity v. The stress τ is composed of two contributions: an elastic term τ^{el} whose *evolution* is explicitly v dependent (one term in the evolution of τ^{el} encodes growth in time proportional to v, representing the stretching of elastic junctions; the other term encodes breaking of junctions), and a viscous term, whose *instantaneous value* is v dependent. Both τ^{el} and τ^{vis} depend on a function $A(\phi)$ that represents the ratio of true to nominal contact area; in this formulation A is not an independently evolving variable, but instead depends monotonically on ϕ.

Two features of this friction law are studied extensively. One is the existence of a minimum in the relation for $\tau(v)$ in steady sliding (constant v, no evolution of ϕ and τ);

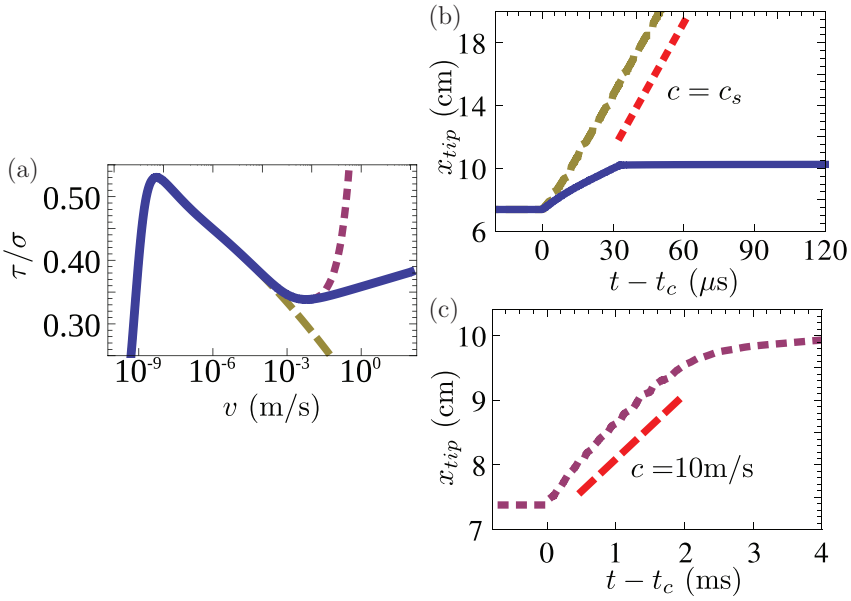

Figure 2.13: Figures illustrating two features of the friction law that are discussed in Section 2.4.3. (a) Friction force in steady sliding for three different friction laws. For the two that revert to velocity strengthening after the velocity weakening branch, note the existence of a local minimum at $v \approx 10^{-2}$ m/s. (b, c) Front tip position as a function of time, showing fronts that are stuck (no motion for some time), then propagate a short distance, then become stuck again. Not to be confused with figures showing fast–slow–fast fronts in time vs position plots, which bear a visual resemblance. In (b), the dashed line shows that under velocity weakening friction with no strengthening branch (the dashed line in (a)), the front propagates at the elastic wave speed and penetrates much deeper into the interface. Figures from Bar-Sinai et al. [6] reprinted with permission from APS. Copyright 2013 by the American Physical Society.

the other is the functional form of the velocity strengthening branch that τ^{vis} gives rise to. The minimum in the steady state friction law is important because a minimum slip velocity required for steady state gives rise to a minimum steady state rupture velocity that they denote $c_{\min}$. This implies that rupture propagating at speed $c < c_{\min}$ is forbidden, an observation that seems to agree with the experimental results of Ben-David et al. [11]. The shape of the velocity strengthening regime strongly influences the propagation speed of transient rupture fronts, which Bar Sinai et al. [5] argue are short-lived excitations of steady-state rupture fronts. For example, a friction law where τ^{vis} is logarithmically strengthening in v supports much faster ruptures than one where τ^{vis} grows linearly with v, see Figure 2.13.

Bouchbinder and co-workers conclude that to understand the rupture fronts, it is crucial to understand the functional form of the steady state friction law, and in [7] they compile experimental data to support their ideas.

2.4.4 Molinari group (FEM)

Molinari and his group have published a series of papers on precursors [49, 68, 69] and rupture fronts in frictional interfaces [47, 48]. The model they use is a 2D (direction of sliding and out-of-plane dimension) elastic [47, 48] or viscoelastic [49, 68, 69] slider interacting with its substrate through a continuum friction law. The slider is represented numerically with a finite element (FEM) discretization. There is some variation in the models between publications, but the friction laws have in common that they are improvements on the simple Amontons–Coulomb friction law. They use a static friction breaking threshold with a coefficient μ_s and a sliding friction level μ_d. However, the transition between the two is not discontinuous and instantaneous upon rupture; instead, they use a slip [49, 68, 69] or velocity [47] weakening law that joins the two levels continuously. They also regularize the change in frictional strength with changes in the normal force [48, 68, 69]. The long-term friction coefficient is proportional to the normal force, but upon changes in normal force that occur fast compared to a characteristic time scale, the frictional strength lags the normal force, that is, it takes some time to increase/decrease the frictional strength. They credit [31, 65] with this Prakash–Clifton law, which they find solves a stability problem exhibited with the unmodified Amontons–Coulomb friction law and allows their solutions to converge with respect to the resolution of the computational mesh.

The details of the external loading conditions strongly affect the frictional dynamics. In [47], which focuses on rupture front propagation, both shear and normal loads were applied through controlling the displacement at the top of the slider. This results in highly non-uniform stress distributions. They investigated the dependence of rupture front speed on local shear to normal stress ratio, evaluated before or during the event, and found that although the stress ratio explained a large part of the front speed, the stress ratio alone did not uniquely determine the speed. See Figure 2.14a.

Finite element methods (FEM) have some advantages over the spring–block models. Among these are freedom in choosing the geometry and the properties of the bulk. They used both elastic and viscoelastic materials (in the latter, the Young modulus varies between a high value during wave propagation and a lower value relevant for static deformations). Also, though they mostly used deformable–rigid interfaces, they recently started investigating deformable–deformable bimaterial interfaces [8, 69]. The viscoelasticity is the main focus in their work on precursors [68, 69], and they find that the relaxation after front arrest allows the regions of elevated shear stress that are created near the end of precursors to persist across multiple events. This in turn affects the local front velocity through its coupling to the shear prestress, see Figure 2.14b.

2.4.5 Braun, Urbakh and co-workers (asperity models)

In the previous sections I described efforts to model rupture fronts in friction using continuum descriptions of the interface interaction. A complementary approach is to include the individual interface junctions in the models. I believe that this level of model is useful for bridging the gap between the individual junction behavior (which is itself a matter of active research) and the macroscale friction dynamics. Even with simple junction behavior laws, complicated macroscale dynamics emerge.

Braun, Urbakh and their co-workers have worked extensively with variants of the so-called earthquake-like model. Because we too have applied a friction model of this

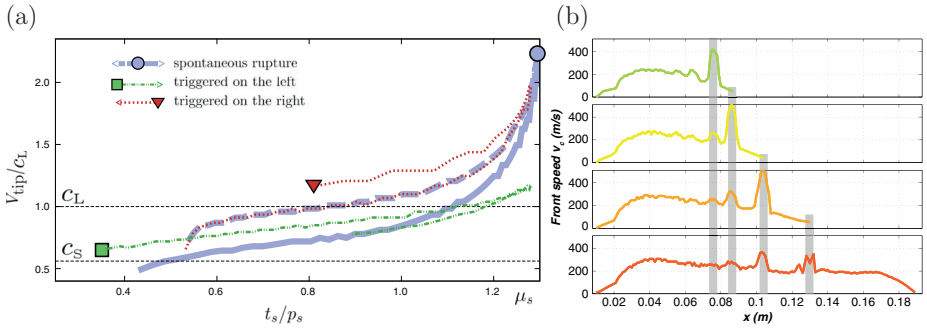

Figure 2.14: Results from FEM simulations by Molinari and his group. (a) The local shear to normal stress ratio at the instant the event starts does not uniquely determine the local rupture front velocity. In the same paper they improve the collapse of the data by replacing the stress ratio with an energy density criterion. (b) The front velocity increases upon reaching regions of elevated shear stress, which persist across events due to the viscoelastic bulk material. From top to bottom are shown the front speed in four successive precursor events. Panel (a) from Kammer et al. [47] reproduced with kind permission from Springer Science and Business Media. © Springer Science+Business Media, LLC 2012. Panel (b) from Radiguet et al. [68] reprinted with permission from APS. Copyright 2013 by the American Physical Society.

The original caption for panel (a) is reproduced here as required by Springer: Three different slip events are presented for the same initial stress state (before triggering or spontaneous initiation). (...) The normalized rupture velocity for all three cases is depicted with respect to the local static ratio of tangential traction t_s to contact pressure p_s (data close to the triggering zone are not shown). Friction parameters are $\mu_s = 1.3$, $\mu_k = 0.6$, and $\alpha = 0.1$ m^2/s^2.

type, I summarize the model of Braun, Urbakh and co-workers in more detail than I did the other models in this section.

Apparently named for originating in or being inspired by the earthquake literature, with the 1967 paper by Burridge and Knopoff [24] at its roots, the earthquake-like model considers a population of junctions that jointly resist the motion of a driven rigid object. The junctions always interact through their combined influence on the slider object, and can also have neighbor and longer-range direct interactions between each other. Typically, each junction can be in either a pinned or a sliding state, with the time spent in the sliding state sometimes considered faster than all other time scales in the problem, and therefore reduced to zero for computational and mathematical convenience [17–21], and sometimes included explicitly [18, 19, 22, 25, 26]. In the pinned state, the junctions act as linear springs, with the individual force resisting the motion of the slider proportional to the elongation of each junction. At a threshold force or threshold elongation (these are equivalent when the force–elongation relation is linear) a pinned junction breaks and enters the sliding state. In the works of Braun, Urbakh and co-workers the threshold varies between junctions. The force contribution from sliding junctions is usually set to zero. When the junction re-enters the pinned state, its lifecycle starts over. If all the junctions have identical properties and no randomness is introduced in their lifecycle, the earthquake-like model organizes into a cycle of breaking and reformation of junctions that recurs indefinitely. In order to

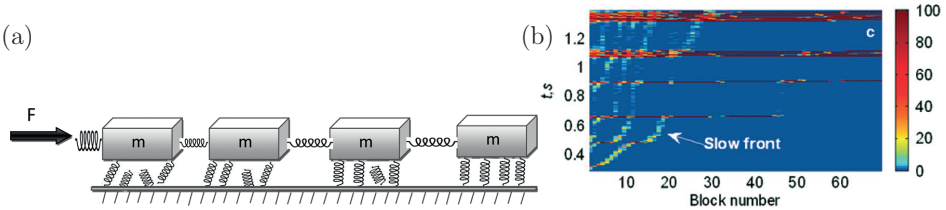

Figure 2.15: Braun, Urbakh and co-workers have studied a 1D chain of blocks, each interacting with the substrate through a population of springs representing microjunctions. (a) Sketch of their model. (b) The fraction of detached contacts, in a time vs position axis. The front labelled as slow occurs on a time scale where the external loading forces increases significantly, and I believe it is of the quasi-static type that I discuss in Publication 1. Figures from Braun et al. [22] reprinted with permission from APS. Copyright 2009 by the American Physical Society.

obtain a non-trivial evolution of the state of the junction population, with time or with sliding history, Braun, Urbakh and co-workers let the strength of each renewed junction be drawn from a probability distribution of strengths. In my publications presented in this thesis, it is the time spent in the slipping state that is drawn from a probability distribution.

The earthquake-like model has a rich range of behavior and has been studied both analytically and numerically. Braun and Peyrard [17, 18, 19] developed a master equation solution for the earthquake-like model applied to a single rigid slider, as a function of the displacement of the slider, expanding on a result by Persson [64]. They found slip stability criteria (stick–slip or smooth sliding appear depending on the relative stiffness of the interface and the loading [17]), studied the effect of thermal activation of bond breaking, and mapped out the velocity dependence of the steady state sliding friction. The master equation complements the works described in the previous sections, which take mesoscale laws as given and study the dynamics on the meso- and macroscales.

Braun et al. [22] used a 1D chain of blocks, each interacting with the interface through an earthquake-like model, to study rupture fronts in a system loaded from the trailing edge. They found that the model supports precursor events and different regimes of rupture fronts. Their slower fronts occur on the same time scale as the increase in the loading force, and may be loading rate dependent. See Figure 2.15. The authors call attention to the way the precursors modify the initially unstressed interface to a highly non-uniform stressed state before the transition to overall sliding occurs. Braun and Peyrard [20] studied propagating rupture kinks in a 1D chain of blocks with the friction governed by their master equation. They triggered ruptures in a uniformly loaded interface and found fronts propagating at velocities about two orders of magnitude slower than the sound speed.

Capozza et al. [25, 26] applied the 1D chain of blocks obeying the earthquake-like model to study other experimental features than rupture fronts. In [25] they studied the influence on the macroscopic static friction of loading the system either from one edge or more uniformly. In [26] they studied how oscillations in the driving force modify the stick–slip cycle on the macroscale. Using a different model where the formation and rupture of junctions is governed by on- and off-rates associated with thermal activation across atomic-scale energy barriers, Filippov et al. and Capozza et al. studied the stability of stick–slip versus steady sliding on the microscale with [27] and without [40]

small amplitude oscillations in the driving. The oscillations significantly reduce the average friction by breaking the first contacts that form, before the interface has time to fully strengthen.

2.4.6 Note on model resolution

Numerical solution schemes for *mathematical* problems are required to converge to a stable solution in the limit of high numerical resolution. The same requirement does not necessarily apply to numerical models of *physical* problems, because as the resolution changes, new aspects of the physical system may become important. For example, Baumberger and Caroli [9] contend that the continuum limit of discretized models of friction is physically irrelevant if the friction description implicitly assumes an average over a large number of contacts.

In the model of Publications 1 and 3, the bulk elastic solver can be taken to high resolution, see Appendix B. However, because the slider–substrate interface in the model is smooth, in the sense that there is no roughness included in the bulk discretization, increasing the resolution of the bulk changes the relative properties of the bulk and the interface. In the continuum limit the springs representing junctions would all lie in a layer thinner than the actual junctions. Well before this point, the sparsity of junctions would have to be included in the model, while at present we assume that all interface blocks interact with the substrate through a large number of junctions. Caroli and Nozières [29] argue that the lower limit of block size in spring–block models of friction is typically much larger than the average intercontact distance.

Even above the limiting resolution, the combined interface and bulk model is not resolution independent. To see this, consider that to keep the net bulk stiffness of the slider constant the inter–block springs' stiffnesses scale as N_x in 1D (N_x is the bulk resolution in the x-direction) and as 1 in 2D, while to keep the net interface stiffness constant the interface springs' stiffnesses scale as $1/N_x$. This means that the local stiffness ratio changes when the resolution changes, and this affects the dynamics. See Publication 4 for more details.

CHAPTER 3

Summary of publications

The publications appear in full later in the thesis. Here I summarize our findings and comment on the relationship between our work and other research in the field. I also comment on how the publications in the thesis relate to each other.

3.1 Publication 1

Publication 1 is [Jørgen Kjoshagen Trømborg, Henrik Andersen Sveinsson, Julien Scheibert, Kjetil Thøgersen, David Skålid Amundsen and Anders Malthe-Sørenssen. Slow slip and the transition from fast to slow fronts in the rupture of frictional interfaces. *Proceedings of the National Academy of Sciences of the United States of America*, **111**, 24 (2014). `http://dx.doi.org/10.1073/pnas.1321752111`].

3.1.1 Summary

Publication 1 introduces our combined multi-junction friction law and 2D spring–block model. In short, the transfer of the external shear and normal loads to the interface occurs through the deformation of the spring–block model, and the frictional interaction between the slider and track are modelled as a set of junctions attached to each interface unit in the bulk discretization. The individual junction law shares many features with that described in Section 2.4.5, the principal differences being that we focus on the effect of a time distribution for junction renewal, and that we assign the friction during slip motion to the junctions rather than to an absolute viscosity acting on the mesoscopic blocks.

We show that the model reproduces both the transitions between fast and slow fronts within a single dynamic rupture event and the short time slip-dynamics observed in the experiments of Fineberg's group [11, 12, 74]. By varying the model parameters to investigate how they affect the rupture fronts we identify slow slip immediately following the arrest of a fast front as a mechanism for the front to propagate further at a much slower pace. We then link slow fronts to slow slip, and demonstrate a proportionality between the slow slip speed behind the front tip and the propagation speed of the front.

Having shown that dynamic slow fronts are possible in the model and arise as part of the spontaneously occurring events when the system is loaded from the side

and driven through a stick–slip cycle, we investigate the conditions under which they are observed. To this end we perform simulations where we either modify or fully construct the distribution of forces in the microscopic junctions. We vary both the shear prestress, which is the average of the forces in a block's junctions, and the width of the force distribution, which controls the local effective static friction threshold, that is, the local strength of the interface. We find that high shear prestress conditions along the whole interface favour fast rupture front propagation, as does low local strength. Conversely, when the initial shear prestress is low or the interface is strong, the fronts that we trigger to study their propagation arrest before reaching the leading edge of the sample. In a strength–prestress diagram, the conditions that lead to front arrest occupy the lower and left regions, while the conditions that lead to fast fronts occupy the upper and right regions. The conditions that lead to dynamic slow fronts, which appear when the fast front propagation stops and the slow slip mechanism takes over and allows the front to propagate further, lie in a band between the arrest and fast front regions. We expect that when this band is narrow, even in experiments or simulations where slow fronts are possible, they will not always be observed.

The slow rupture fronts in the model result from slow slip, but the microscopic origin of the slow slip is not crucial to this result. To show this, we change the friction law by replacing the ensemble of junctions for each block with a single junction that has slow slip after rupture as a control parameter. We find very similar results in this simplified model, including spontaneously occurring events with fast-slow transitions and the same proportionality between slip speed and front speed.

3.1.2 Comparison to other work

As described in Section 2.4 there are other groups working on theory and simulations for rupture fronts. Here I very briefly compare our publication to their work. The main new results are that our simulations spontaneously produce both slow and fast rupture fronts and the transitions between them. This allows us to identify a mechanism for the transition from fast to slow fronts.

Quasistatic fronts propagate because of changes in the external load, and they stop when the driving stops. Dynamic fronts, which can be slow or fast, are triggered either manually or by changes in the external load, but once they start propagating, they are self-sustaining and continue also without further increase of the external driving. This distinction sheds light on the difference between our results and the results in the models described in Section 2.4. Urbakh and coworkers [22, 25] used 1D spring–block models with an interfacial behavior also based on micro-junctions having two possible states. However, their model did not have a mechanism that generated slow slip. As a consequence, they observed fast and quasistatic fronts, but did not observe dynamic slow fronts like those reported in Publication 1. Bouchbinder and coworkers [5, 6, 15] have developed an improved rate-and-state law and used it in 1D. They consider the classical aging timescale whereas we consider a dynamic healing timescale relevant during the short-lived rupture-induced temperature rise of the interface. They observed the transition from quasistatic to fast dynamic rupture, but no fast-to-slow dynamic front transition. The groups using 2D models and velocity-weakening local friction laws [47, 62] observed fast and quasistatic fronts, but they did not report any transition from fast to slow dynamic fronts.

Our results make a direct bridge between the separate observations of a transition from fast to slow fronts and of slow slip in recent experiments [12, 74]. As slow slip was

observed in many systems from geoscience [45, 59, 63] to materials science [12, 44], we expect the transition to slow fronts to be possible in these systems, too.

3.2 Publication 2

Publication 2 is [Kjetil Thøgersen, Jørgen Kjoshagen Trømborg, Henrik Andersen Sveinsson, Anders Malthe-Sørenssen and Julien Scheibert. History-dependent friction and slow slip from time-dependent microscopic junction laws studied in a statistical framework. *Physical Review E*, **89**, 052401 (2014). `http://dx.doi.org/10.1103/PhysRevE.89.052401`].

3.2.1 Summary

Where Publication 1 is concerned with the dynamics of the 2D system, Publication 2 is concerned with how the friction depends on the slip dynamics. We therefore take a single interface block and its junctions as our system, and develop analytical and numerical results for the friction force on the block.

The framework we introduce describes the collective behavior of a large number of micro-junctions. Each micro-junction can switch in time between two states: a pinned state characterized by a displacement-controlled force and a slipping state characterized by a time-dependent force. Instead of tracking each micro-junction individually, the state of the interface is described by two coupled distributions for (i) the stretching of pinned junctions and (ii) the time spent in the slipping state. This framework allows for a whole family of micro-junction behavior laws, and we show how it represents an overarching structure for many existing models found in the friction literature, including the law introduced in Publication 1. We then use this framework to pinpoint the effects of the time scale that controls the duration of the slipping state. The model reproduces a series of friction phenomena that are observed experimentally. The macroscopic steady state friction force can be calculated analytically. It is velocity dependent, either monotonic (strengthening or weakening) or non-monotonic (weakening-strengthening) depending on the microscopic behavior of the individual junctions.

The steady state is only reached when the slip speed of the slider is constant, and in general this is not the case. While the steady state solutions are also reasonable approximations in some limits, an understanding of transients is particularly important to the study of a large variety of frictional situations, including oscillating contacts [71]; the onset of frictional sliding, be it quasi-static [67] or dynamic [74]; the cessation of slip [12]; and friction instabilities [54]. We therefore study the evolution of the friction with onset and cessation of motion and find that the model predicts a non-trivial history dependence of the local static friction threshold. Namely, the more abruptly the slider stops in one event, the larger is the static friction threshold in the next event. Here we use the deceleration value in a prescribed slip profile to quantify the abruptness of slider arrest; in Publication 3 we introduce a more generally applicable quantifier. We suggest that this form of history dependence should be investigated in experiments, and we provide the acceleration range in which the effect is expected to be experimentally observable.

3.2.2 Comparison to other work

Section IIC of Publication 2 is a detailed comparison to other work. Basically, the mathematical framework we introduce is an overarching structure for the models in [17, 18, 22, 25, 26, 39]. Braun and Peyrard [17, 18] studied the effect of disorder in the junction strength in great detail. We refer the reader to their work, and instead focus on the effect of disorder in the time for junction renewal. We were directly inspired by the calculations in [17, 18], and adapted them to consider two coupled distributions rather than just one. The additional complications arising from the coupling between the distributions meant that we did not formulate a master equation for the junction distributions. However, the additional richness of the junction law did result in a richer steady state behavior, and it allowed us to place more emphasis on the coupling between the slider motion and the junction evolution.

3.3 Publication 3

Publication 3 is [Jørgen Kjoshagen Trømborg, Henrik Andersen Sveinsson, Kjetil Thøgersen, Julien Scheibert and Anders Malthe-Sørenssen. Speed of fast and slow rupture fronts along frictional interfaces. In review in *Physical Review E*].

3.3.1 Summary

Publication 3 builds on and extends the results of Publication 1. The two publications share the same main model: 2D spring–block bulk elasticity and a large number of interface springs representing micro-junctions to model the friction.

To make Publication 3 self-contained, and to present results that were left out of Publication 1 because of length limitations, Publication 3 begins by expanding on and providing additional interpretations of the main findings in Publication 1. We show the loading curve, example front dynamics and example slip dynamics. We then identify a signature of slow fronts that can be seen in the macroscopic loading curve, which potentially simplifies the search for slow fronts in experiments. We argue the difference between fast and slow fronts in the model by showing that the fast slip and fast front speeds scale with inertia ($\sqrt{\rho}$) while the slow slip and slow front speeds do not change with changes to the mass density ρ.

We find that a proportionality between material slip speed and rupture front speed, reported for slow fronts in Publication 1, actually holds across the full range of front speeds we observe. We highlight the long transients in front speed even in homogeneous interfaces, and we study how both the local shear to normal stress ratio and the local strength are involved in the selection of front type and front speed. Higher shear prestress and weaker interfaces favour faster front propagation.

In Publication 2 we studied how the friction force on an interface block depends on the block's slip dynamics in cases where the slip dynamics could be readily characterized. Here we study this dependence when the block slip dynamics arises from the full complexity of the model. We focus on how the cessation of slip in one event sets up the distribution of micro-junction forces that determines the effective local strength in the next event. To characterize the complicated slip dynamics we introduce an experimentally accessible integrated measure of block slip history, the Gini coefficient. The Gini coefficient is commonly used to characterize the inequality of the income or wealth distribution in a population [41, 42], but can be applied to our case without

modification. We use the Gini coefficient to characterize the inequality of slip motion in time during cessation of slip, and we demonstrate that in the model it is a good predictor of the history-dependent local static friction coefficient of the interface.

The results in Publication 3 will contribute both to building a physically-based classification of the various types of fronts and to identifying the important mechanisms involved in the selection of their propagation speed.

3.3.2 Comparison to other work

In Publication 1 we mainly reported on the existence of slow and fast rupture fronts and the transitions between them. In Publication 3 we go beyond this by systematically studying how the rupture speed, be it fast or slow, varies with material parameters and initial conditions.

The experiments of Ben-David et al. [11] showed an increase in local front speed with increasing local shear to normal stress ratio τ/p. The large scatter in the data indicates that the local stress ratio is not sufficient on its own to predict the local front speed. Kammer et al. [47], in their simulations, proposed an energetic criterion to replace the stress ratio, but this too did not fully collapse their data. Bar Sinai et al. [5], studying homogeneous interfaces, found an increasing front speed with increasing shear prestress, in their case normalized against a characteristic shear stress rather than the normal stress. Their results fall on a single line with no scatter. We find in Publication 3 that in addition to the shear to normal stress ratio, which is indeed an important influence on the rupture front speed, (i) the front speed in the model is transient even in homogeneous interfaces, so the local conditions alone do not determine the local front speed, and (ii) front speed depends also on the local strength, which probably shows significant variation in experiments. These are candidate explanations for the scatter in the experimental data.

In Bar Sinai et al. [5], the slow slip speed was selected as the speed for which the steady-state friction law had a minimum. However, the existence of such a minimum is not a necessary condition for slow fronts to appear in a system. As a matter of fact, in our model, and for the parameters used, the steady state friction law is purely decreasing. The apparent contradiction disappears as soon as one remembers that in our model, the slow slip speed arises from a completely different physical mechanism, namely the time distributed relaxation of the interface after its rupture and arrest.

To our knowledge we are the first to use the Gini coefficient to relate the cessation of slip in one event to the local strength of the interface in the following event. Of course, the explicit time dependence in the microscopic junction law lends itself particularly well to this analysis, because it gives a direct coupling between the block slip history and the junction force distribution. However, it will be interesting to see if the Gini coefficient finds applicability also in simulations or experiments where the link between block slip and junction state is more indirect.

3.4 Publication 4

Publication 4 is [David Skålid Amundsen, Kjetil Thøgersen, Jørgen Kjoshagen Trømborg, Eytan Katzav, Anders Malthe-Sørenssen and Julien Scheibert. Steady-state propagation speed of rupture fronts along 1D frictional interfaces. *In preparation*].

3.4.1 Summary

Publication 4 returns to the 1D model. This work was started before the work reported in Publications 1–3, but because David Skålid Amundsen (the first author) left the University of Oslo after getting his MSc, to do his PhD in astrophysics, the publication was delayed.

In Publication 3 the transients in rupture front speed were as long or longer than the slider being simulated. In the simulations in Publication 4 we increase the system length and use extrapolation to infinity to study the converged (steady state) front speeds. The length of the transients goes down as the prestress goes up. We also solve for the converged front speed directly from the equations of motion numerically (without simulations), and, in a couple of special cases, analytically. In the model, the rupture fronts converge to speeds faster than the 1D sound speed, and the steady state front speed diverges as the shear prestress approaches the local static friction threshold. This divergence is a known result [51] and results from the experimentally unlikely scenario that every contact is loaded arbitrarily close to its breaking threshold before the rupture starts.

As part of the calculations we identify, within the model, the dimensionless parameters that control the front speed. They are: the shear prestress normalized with the static and dynamic friction levels; a bulk viscosity normalized with a critical damping value; and the interfacial to bulk stiffness ratio. We perform a systematic study of the influence on front speed of these parameters. We find that the steady state front speed is always an increasing function of the shear prestress. Increases in the bulk viscosity, which counteracts relative motion of neighbouring blocks, increase the steady state front speed. The interfacial to bulk stiffness ratio also exhibits the same trend, with stiffer interfaces corresponding to higher front speeds.

3.4.2 Comparison to other work

The 1D spring–block model is a popular model. In its fully dynamic (as opposed to cellular automaton) form it has been used to model not only friction [e.g. 1, 20, 22, 25, 26, 55, 64, 82] and earthquake dynamics [e.g. 24, 28], but also, among others, self-organized criticality in nonequilibrium systems with many degrees of freedom [e.g. 35], fluctuations in dissipative systems [e.g. 4] and creep in granular materials [e.g. 14].

We believe that Publication 4, with its systematic exploration of the effect of the interfacial stiffness and the bulk viscosity, will provide useful knowledge for future studies using this model.

CHAPTER 4

Outlook

In this chapter I outline opportunities for future research.

I think that an important goal in the field of friction is to come up with a model that predicts the frictional properties of an interface from the bottom up. That is, given information about the surface chemistry and topography of both sides of the interface, as well as the bulk equation of state and the detailed loading conditions, the model would predict the frictional dynamics. This thesis is my contribution towards this larger goal. From this point of view, it is clear that a much needed, but potentially very difficult step is to determine from its building blocks, via experiment, simulations and theory, the evolution law of a single micro-junction. Because frictional systems are very diverse in their interface composition and structure, I believe that the answers will be strongly system-dependent. Nevertheless, we can strive for a common framework with which to tackle the question of single asperity behavior.

In principle, single junction behavior could be determined by fully atomistic simulations. This would complement experiments by providing full spatiotemporal resolution. However, atomistic models are limited by the short timescales that they can access. A good overview of atomistic simulations in tribology is given by Vanossi et al. [82, Section III], who estimate that on a medium-size parallel computer of ca. 10^2 cores running at 10^9 floating point operations per second per core, a simulation with 10^5 atoms, a modest number, being smaller than a cube of side 100 atoms, can progress at approximately 1 µs per simulation day. Larger systems require a larger computer or progress even slower. A typical junction size is 1 µm and typical inter-atomic distances are in the range of a few angstroms, so that to resolve a junction atomistically requires on the order of $(1\ \mu\text{m}/3\ \text{Å})^3 \sim 10^{10}$ atoms, so that even at macroscopic sliding speeds of order 1 m/s, it is infeasible to simulate even a single rupture event where one micrometer-sized junction moves past another. There is a need for coarse-grained models that are themselves founded on atomistic simulations, but which bring the length- and timescales of real junctions within the currently accessible range.

An alternative and promising approach to the difficult problem of determining the appropriate micro-junction evolution laws for a given experimental system is to circumvent the problem by bringing the experimental junctions to the meso- or macroscale. A popular system is rubber-on-glass, with patterns of contacts created on the glass or on the rubber. Poly(dimethyl siloxane) (PDMS) is frequently used. PDMS on glass is also used with microscopic patterns, but I am here interested in the larger-scale patterns such as in the work of Romero et al. [72], with whom we have an informal collaboration.

They create a pattern of half-spheres of PDMS on a flat PDMS back layer and study the friction against a smooth glass plate. Imaging in transmission allows them to determine the size of each true contact, the position of the center of true contact and the center of the equatorial plane of each half-sphere where it attaches to the back layer, for each half-sphere. Because the PDMS is soft and smooth (below the length scale of the half-spheres) and the glass is smooth, there is full contact within the contact region of each half-sphere. Because the asperities are shaped as half-spheres, Hertz' theory allows calculation of the shear and normal forces on each asperity, at least for small deformations. In practice the deformations are rather large compared to the size of the half-spheres. However, the raw contact size and deformation measurements can be used to formulate an asperity evolution law *directly from the data*, without going through Hertz' or another theory, that can be applied as the smallest scale in simulations of this system. The idea is this: The strength of each asperity depends on its true contact size. For each asperity, measure its true contact size, the deformation at which it starts slipping, and the deformation to which it relaxes. The soft-on-stiff, patterned-on-smooth setup ensures that each asperity stays intact and can be tracked throughout the experiment. Tabulate or fit an equation to this strength vs size data. The table or fit is the friction law for these asperities. We are currently pursuing this approach.

One of the main ideas investigated in this thesis is the strong link between slow slip and slow fronts. I have focused on the experimental results of Fineberg's group, but the topic of slow slip has much wider interest [33, 44, 45, 60, 61, 63, 84, 86]. Slow slip is observed in crustal earthquakes [45, 63] and during hydraulic fracturing for shale gas extraction [33, 86]. Models of these systems should include mechanisms for slow slip. It would be interesting to see it the slow slip in these models and experiments are linked with the slow propagation of rupture fronts as well. This data may not be part of the experimental record yet, but should be readily accessible in the simulations.

The traditional zero-dimensional friction theories describe a rigid object moving on a non-deforming substrate. In this thesis, and in work by many other authors, some of it described in Section 2.4, the sliding object is imbued with more detail. It can deform in one, two or three dimensions, it is elastic or viscoelastic [68], and it couples to the interface through a continuum law or a collection of micro-junctions. This allowed the models to reproduce and bring additional insights into the rich spatiotemporal dynamics observed in experiments that monitor the mesoscale. However, this approach, in which the slider is treated in greater detail, but the substrate is still considered to be an unchanging wall against which the friction takes place, breaks the symmetry in the description. When the slider is rigid, in fact usually point-like, a non-deforming substrate is perfectly adequate. When the slider is a deformable object acted upon by external loads carefully matched to the experimental loading conditions, it would be more appropriate to treat the substrate in the same detailed way, as is done by e.g. [8, 69]. It has been and will remain useful to consider an elaborate slider and a simple track, but I believe that moving to a not too elaborate slider and a similarly detailed track will bring additional insights that are otherwise inaccessible. Of course, for modelling systems where there is a real asymmetry in the properties of the opposing surfaces, like a patterned rubber against a smooth glass, an asymmetric description will be justified, being in this case of physical origin rather than a modelling convenience.

Linear elastic fracture mechanics (LEFM) is a well-developed theory for the bulk fracture of brittle materials. The study of frictional rupture leads naturally to asking how well LEFM applies to the friction problem. This is an important question because

(i) much of the work on earthquakes that involve frictional slip along faults apply LEFM [13, 79], and (ii) LEFM may provide new insights in friction. In 2014, Svetlizky and Fineberg [80] measured the strain components at points near a PMMA–PMMA interface during frictional rupture and found good agreement with LEFM. Kammer et al. [49] took LEFM as the basis for a theory to predict the length of precursors in the experiments of Rubinstein et al. [76], mentioned in Section 2.4.2. In both these works the LEFM result is compared to the experiment or simulation on a point-by-point basis (the location of the sensors in [80], and the precursor arrest length in [49]). For 2D and 3D simulations it would be interesting to also compare the stress and strain fields in the whole sample to the LEFM result. This could tie in with the previous paragraph's discussion by assessing the importance of modelling a truly bi-material interface rather than a deformable–rigid interface.

One of the findings of my work (also seen by others) is that much of the complexity in the frictional dynamics arise directly from the geometry of the samples and the loading conditions. This is encouraging from a modelling and friction design point of view, but also suggests limitations to what we can achieve. On the modelling side, the bulk properties and loading conditions benefit from a strong knowledge base from the mathematics, physics and engineering of non-moving structures. Consequently, even for multilayered and complicated experimental geometries, once they are known, bulk and load modelling is a question of acquiring and adapting the existing tools rather than developing new ones. This should allow the focus to be directed towards the frictional interface itself. On the friction design side, it is promising that experiments show strong dependence of the friction on external geometric conditions, because these can be controlled and adjusted independently of the manufacture and conditioning of the interface. The flip side of this coin is that controlling the interface may not be enough to get the frictional behavior that you seek in your application: you may have to keep friction in mind when you design the surrounding load and geometry too.

Bibliography

[1] D. S. Amundsen, J. Scheibert, K. Thøgersen, J. Trømborg, and A. Malthe-Sørenssen. 1D model of precursors to frictional stick-slip motion allowing for robust comparison with experiments. *Tribol. Lett.*, 45(2):357–369, 2012. URL http://dx.doi.org/10.1007/s11249-011-9894-3.

[2] J. F. Archard. Elastic deformation and the laws of friction. *Proc. R. Soc. London, Ser. A*, 243(1233):190–205, 1957. URL http://www.jstor.org/stable/100445.

[3] M. C. Audry, C. Fretigny, A. Chateauminois, J. Teissere, and E. Barthel. Slip dynamics at a patterned rubber/glass interface during stick-slip motions. *Eur. Phys. J. E*, 35(9), 2012. URL http://dx.doi.org/10.1140/epje/i2012-12083-0.

[4] S. Aumaître, S. Fauve, S. McNamara, and P. Poggi. Power injected in dissipative systems and the fluctuation theorem. *Eur. Phys. J. B*, 19(3):449–460, 2001. URL http://dx.doi.org/10.1007/s100510170321.

[5] Y. Bar Sinai, E. A. Brener, and E. Bouchbinder. Slow rupture of frictional interfaces. *Geophys. Res. Lett.*, 39(3):L03308, 2012. URL http://dx.doi.org/10.1029/2011GL050554.

[6] Y. Bar-Sinai, R. Spatschek, E. A. Brener, and E. Bouchbinder. Instabilities at frictional interfaces: Creep patches, nucleation, and rupture fronts. *Phys. Rev. E*, 88(6):060403, 2013. URL http://link.aps.org/doi/10.1103/PhysRevE.88.060403.

[7] Y. Bar-Sinai, R. Spatschek, E. A. Brener, and E. Bouchbinder. On the velocity-strengthening behavior of dry friction. *J. Geophys. Res.: Solid Earth*, 119(3):1738–1748, 2014. URL http://dx.doi.org/10.1002/2013JB010586.

[8] F. Barras, D. S. Kammer, P. H. Geubelle, and J.-F. Molinari. A study of frictional contact in dynamic fracture along bimaterial interfaces. *Int. J. Fract.*, 189(2):149–162, 2014. URL http://dx.doi.org/10.1007/s10704-014-9967-z.

[9] T. Baumberger and C. Caroli. Solid friction from stick–slip down to pinning and aging. *Adv. Phys.*, 55(3-4):279–348, 2006. URL http://www.tandfonline.com/doi/abs/10.1080/00018730600732186.

[10] T. Baumberger, C. Caroli, and O. Ronsin. Self-healing slip pulses along a gel/glass interface. *Phys. Rev. Lett.*, 88(7):075509, 2002. URL http://link.aps.org/doi/10.1103/PhysRevLett.88.075509.

[11] O. Ben-David, G. Cohen, and J. Fineberg. The dynamics of the onset of frictional slip. *Science*, 330(6001):211–214, 2010. URL http://www.sciencemag.org/content/330/6001/211.abstract.

[12] O. Ben-David, S. M. Rubinstein, and J. Fineberg. Slip-stick and the evolution of frictional strength. *Nature*, 463(7277):76–79, 2010. URL http://dx.doi.org/10.1038/nature08676.

[13] Y. Ben-Zion. Collective behavior of earthquakes and faults: Continuum-discrete transitions, progressive evolutionary changes, and different dynamic regimes. *Rev. Geophys.*, 46(4):RG4006, 2008. URL http://dx.doi.org/10.1029/2008RG000260.

[14] B. Blanc, J.-C. Géminard, and L. A. Pugnaloni. On-and-off dynamics of a creeping frictional system. *Eur. Phys. J. E*, 37(11):112, 2014. URL http://dx.doi.org/10.1140/epje/i2014-14112-4.

[15] E. Bouchbinder, E. A. Brener, I. Barel, and M. Urbakh. Slow cracklike dynamics at the onset of frictional sliding. *Phys. Rev. Lett.*, 107(23):235501, 2011. URL http://dx.doi.org/10.1103/PhysRevLett.107.235501.

[16] F. P. Bowden and D. Tabor. *The Friction and Lubrication of Solids*. Clarendon Press, Oxford, 2001. First published 1950.

[17] O. M. Braun and M. Peyrard. Modeling friction on a mesoscale: Master equation for the earthquakelike model. *Phys. Rev. Lett.*, 100:125501, 2008. URL http://dx.doi.org/10.1103/PhysRevLett.100.125501.

[18] O. M. Braun and M. Peyrard. Master equation approach to friction at the mesoscale. *Phys. Rev. E*, 82:036117, 2010. URL http://dx.doi.org/10.1103/PhysRevE.82.036117.

[19] O. M. Braun and M. Peyrard. Dependence of kinetic friction on velocity: Master equation approach. *Phys. Rev. E*, 83(4 Pt 2):046129, 2011. URL http://dx.doi.org/10.1103/PhysRevE.83.046129.

[20] O. M. Braun and M. Peyrard. Crack in the frictional interface as a solitary wave. *Phys. Rev. E*, 85(2):026111, 2012. URL http://link.aps.org/doi/10.1103/PhysRevE.85.026111.

[21] O. M. Braun and J. Röder. Transition from stick-slip to smooth sliding: An earthquakelike model. *Phys. Rev. Lett.*, 88(9):096102, 2002. URL http://dx.doi.org/10.1103/PhysRevLett.88.096102.

[22] O. M. Braun, I. Barel, and M. Urbakh. Dynamics of transition from static to kinetic friction. *Phys. Rev. Lett.*, 103(19):194301, 2009. URL http://prl.aps.org/abstract/PRL/v103/i19/e194301.

[23] K. Brörmann, I. Barel, M. Urbakh, and R. Bennewitz. Friction on a microstructured elastomer surface. *Tribol. Lett.*, 50(1):3–15, 2013. URL http://link.springer.com/10.1007/s11249-012-0044-3.

[24] R. Burridge and L. Knopoff. Model and theoretical seismicity. *Bull. Seismol. Soc. Am.*, 57(3):341–371, 1967. URL http://www.bssaonline.org/content/57/3/341.abstract.

[25] R. Capozza and M. Urbakh. Static friction and the dynamics of interfacial rupture. *Phys. Rev. B*, 86(8):085430, 2012. URL http://link.aps.org/doi/10.1103/PhysRevB.86.085430.

[26] R. Capozza, S. M. Rubinstein, I. Barel, M. Urbakh, and J. Fineberg. Stabilizing stick-slip friction. *Phys. Rev. Lett.*, 107(2):024301, 2011. URL http://link.aps.org/doi/10.1103/PhysRevLett.107.024301.

[27] R. Capozza, I. Barel, and M. Urbakh. Probing and tuning frictional aging at the nanoscale. *Sci. Rep.*, 3:1896, 2013. URL http://dx.doi.org/10.1038/srep01896.

[28] J. M. Carlson, J. S. Langer, and B. E. Shaw. Dynamics of earthquake faults. *Rev. Mod. Phys.*, 66(2):657–670, 1994. URL http://dx.doi.org/10.1103/RevModPhys.66.657.

[29] C. Caroli and P. Nozières. Hysteresis and elastic interactions of microasperities in dry friction. *Eur. Phys. J. B*, 4(2):233–246, 1998. URL http://link.springer.com/article/10.1007/s100510050374.

[30] A. Chateauminois, C. Fretigny, and L. Olanier. Friction and shear fracture of an adhesive contact under torsion. *Phys. Rev. E*, 81(2):026106, 2010. URL http://link.aps.org/doi/10.1103/PhysRevE.81.026106.

[31] A. Cochard and J. R. Rice. Fault rupture between dissimilar materials: Ill-posedness, regularization, and slip-pulse response. *J. Geophys. Res.: Solid Earth*, 105(B11):25891–25907, 2000. URL http://dx.doi.org/10.1029/2000JB900230.

[32] C. A. Coulomb. *Théorie des machines simples*. Bachelier, Librairie Quai des Augustins, Paris, 1821.

[33] I. Das and M. D. Zoback. Long-period, long-duration seismic events during hydraulic fracture stimulation of a shale gas reservoir. *The Leading Edge*, 30(7):778–786, 2011. URL http://library.seg.org/doi/abs/10.1190/1.3609093.

[34] D. Dawson. *History of Tribology*. Professional Engineering Publishing Limited, London and Bury St Edmunds, United Kingdom, second edition, 1998.

[35] M. de Sousa Vieira. Self-organized criticality in a deterministic mechanical model. *Phys. Rev. A*, 46(10):6288–6293, 1992. URL http://dx.doi.org/10.1103/PhysRevA.46.6288.

[36] J. Dieterich. Time-dependent friction and the mechanics of stick-slip. *Pure Appl. Geophys.*, 116(4-5):790–806, 1978. URL http://dx.doi.org/10.1007/BF00876539.

[37] J. H. Dieterich. Time-dependent friction in rocks. *J. Geophys. Res.*, 77(20):3690–3697, 1972. URL http://dx.doi.org/10.1029/JB077i020p03690.

[38] J. H. Dieterich. Modeling of rock friction: 1. Experimental results and constitutive equations. *J. Geophys. Res.*, 84(B5):2161–2168, 1979. URL http://dx.doi.org/10.1029/JB084iB05p02161.

[39] Z. Farkas, S. R. Dahmen, and D. E. Wolf. Static versus dynamic friction: the role of coherence. *J. Stat. Mech.: Theory Exp.*, 2005(06):P06015, 2005. URL http://iopscience.iop.org/1742-5468/2005/06/P06015.

[40] A. E. Filippov, J. Klafter, and M. Urbakh. Friction through dynamical formation and rupture of molecular bonds. *Phys. Rev. Lett.*, 92(13):135503, 2004. URL http://dx.doi.org/10.1103/PhysRevLett.92.135503.

[41] G. M. Giorgi. Bibliographic portrait of the Gini concentration ratio. *METRON: International Journal of Statistics*, XLVIII:183–221, 1990. URL http://econpapers.repec.org/RePEc:wpa:wuwpem:0511004.

[42] G. M. Giorgi. Income inequality measurement: The statistical approach. In J. Silber, editor, *Handbook on Income Inequality Measurement*, chapter 8, pages 245–267. Kluwer Academic Publishers, New York, 1999. URL http://dx.doi.org/10.1007/978-94-011-4413-1.

[43] J. A. Greenwood and J. B. P. Williamson. Contact of nominally flat surfaces. *Proc. R. Soc. London, Ser. A*, 295(1442):300–319, 1966. URL http://dx.doi.org/10.1098/rspa.1966.0242.

[44] F. Heslot, T. Baumberger, B. Perrin, B. Caroli, and C. Caroli. Creep, stick-slip, and dry-friction dynamics: Experiments and a heuristic model. *Phys. Rev. E*, 49 (6):4973–4988, 1994. URL http://link.aps.org/doi/10.1103/PhysRevE.49.4973.

[45] H. Hirose and K. Obara. Repeating short- and long-term slow slip events with deep tremor activity around the Bungo channel region, southwest Japan. *Earth Planets Space*, 57(10):961–972, 2005. URL http://dx.doi.org/10.1186/BF03351875.

[46] K. L. Johnson. *Contact mechanics*. Cambridge University Press, Cambridge, 1985.

[47] D. S. Kammer, V. A. Yastrebov, P. Spijker, and J.-F. Molinari. On the propagation of slip fronts at frictional interfaces. *Tribol. Lett.*, 48(1):27–32, 2012. URL http://dx.doi.org/10.1007/s11249-012-9920-0.

[48] D. S. Kammer, V. A. Yastrebov, G. Anciaux, and J. F. Molinari. The existence of a critical length scale in regularised friction. *J. Mech. Phys. Solids*, 63:40–50, 2014. URL http://www.sciencedirect.com/science/article/pii/S0022509613002159.

[49] D. S. Kammer, M. Radiguet, J.-P. Ampuero, and J.-F. Molinari. Linear elastic fracture mechanics predicts the propagation distance of frictional slip. *Tribol. Lett.*, 57(23), 2015. URL http://dx.doi.org/10.1007/s11249-014-0451-8.

[50] Y. Katano, K. Nakano, M. Otsuki, and H. Matsukawa. Novel friction law for the static friction force based on local precursor slipping. *Sci. Rep.*, 4:6324, 2014. URL http://dx.doi.org/10.1038/srep06324.

[51] L. Knopoff. Noncausality of numerical models of dynamic fracture growth. *Ann. Geofis.*, XL(5):1287—-1292, 1997. URL http://dx.doi.org/10.4401/ag-3873.

[52] L. D. Landau and E. M. Lifshitz. Theory of elasticity. In *Course of Theoretical Physics*, volume 7. Pergamon Press, Oxford, third edition, 1986. First English edition 1959.

[53] H. P. Langtangen. *Computational Partial Differential Equations: Numerical Methods and Diffpack Programming*. Springer, Berlin, second edition, 2002.

[54] J. Le Rouzic, A. Le Bot, J. Perret-Liaudet, M. Guibert, A. Rusanov, L. Douminge, F. Bretagnol, and D. Mazuyer. Friction-induced vibration by Stribeck's law: Application to wiper blade squeal noise. *Tribol. Lett.*, 49(3):563–572, 2013. URL http://dx.doi.org/10.1007/s11249-012-0100-z.

[55] S. Maegawa, A. Suzuki, and K. Nakano. Precursors of global slip in a longitudinal line contact under non-uniform normal loading. *Tribol. Lett.*, 38(3):313–323, 2010. URL http://dx.doi.org/10.1007/s11249-010-9611-7.

[56] C. Marone. Laboratory-derived friction laws and their application to seismic faulting. *Annu. Rev. Earth Planet. Sci.*, 26(1):643–696, 1998. URL http://www.annualreviews.org/doi/abs/10.1146/annurev.earth.26.1.643.

[57] L. Monette and M. P. Anderson. Elastic and fracture properties of the two-dimensional triangular and square lattices. *Modell. Simul. Mater. Sci. Eng.*, 2(1):53, 1994. URL http://stacks.iop.org/0965-0393/2/i=1/a=004.

[58] S. Nielsen, J. Taddeucci, and S. Vinciguerra. Experimental observation of stick-slip instability fronts. *Geophys. J. Int.*, 180(2):697–702, 2010. URL http://dx.doi.org/10.1111/j.1365-246X.2009.04444.x.

[59] M. Ohnaka and Y. Kuwahara. Characteristic features of local breakdown near a crack-tip in the transition zone from nucleation to unstable rupture during stick-slip shear failure. *Tectonophysics*, 175(1-3):197–220, 1990. URL http://www.sciencedirect.com/science/article/pii/004019519090138X.

[60] M. Ohnaka and T. Yamashita. A cohesive zone model for dynamic shear faulting based on experimentally inferred constitutive relation and strong motion source parameters. *J. Geophys. Res.*, 94(B4):4089–4104, 1989. URL http://doi.wiley.com/10.1029/JB094iB04p04089.

[61] M. Ohnaka, Y. Kuwahara, and K. Yamamoto. Constitutive relations between dynamic physical parameters near a tip of the propagating slip zone during stick-slip shear failure. *Tectonophysics*, 144(1-3):109–125, 1987. URL http://dx.doi.org/10.1016/0040-1951(87)90011-4.

[62] M. Otsuki and H. Matsukawa. Systematic breakdown of Amontons' law of friction for an elastic object locally obeying Amontons' law. *Sci. Rep.*, 3:1586, 2013. URL http://dx.doi.org/10.1038/srep01586.

[63] Z. Peng and J. Gomberg. An integrated perspective of the continuum between earthquakes and slow-slip phenomena. *Nat. Geosci.*, 3(9):599–607, 2010. URL http://dx.doi.org/10.1038/ngeo940.

[64] B. N. J. Persson. Theory of friction: Stress domains, relaxation, and creep. *Phys. Rev. B*, 51(19):13568–13585, 1995. URL http://link.aps.org/doi/10.1103/PhysRevB.51.13568.

[65] V. Prakash and R. J. Clifton. Time resolved dynamic friction measurements in pressure-shear. In K. Ramesh, editor, *Experimental Techniques in the Dynamics of Deformable Solids*, volume AMD-165, pages 33–48, New York, 1993. American Society of Mechanical Engineers. URL http://www.scopus.com/inward/record.url?eid=2-s2.0-0027188916&partnerID=tZOtx3y1.

[66] W. H. Press, S. A. Teukolsky, W. T. Vetterling, and B. P. Flannery. *Numerical Recipes*. Cambridge University Press, New York, third edition, 2007.

[67] A. Prevost, J. Scheibert, and G. Debrégeas. Probing the micromechanics of a multi-contact interface at the onset of frictional sliding. *Eur. Phys. J. E*, 36(2): 17, 2013. URL http://dx.doi.org/10.1140/epje/i2013-13017-0.

[68] M. Radiguet, D. S. Kammer, P. Gillet, and J.-F. Molinari. Survival of heterogeneous stress distributions created by precursory slip at frictional interfaces. *Phys. Rev. Lett.*, 111:164302, 2013. URL http://dx.doi.org/10.1103/PhysRevLett.111.164302.

[69] M. Radiguet, D. S. Kammer, and J. F. Molinari. The role of viscoelasticity on heterogeneous stress fields at frictional interfaces. *Mech. Mater.*, 80, Part B(SI): 276–287, 2015. URL http://www.sciencedirect.com/science/article/pii/S0167663614000520.

[70] J. Rice and A. Ruina. Stability of steady frictional slipping. *J. Appl. Mech.*, 50 (2):343–349, 1983. URL http://dx.doi.org/doi:10.1115/1.3167042.

[71] E. Rigaud, D. Mazuyer, and J. Cayer-Barrioz. An interfacial friction law for a circular EHL contact under free sliding oscillating motion. *Tribol. Lett.*, 51(3): 419–430, 2013. URL http://dx.doi.org/10.1007/s11249-013-0177-z.

[72] V. Romero, E. Wandersman, G. Debrégeas, and A. Prevost. Probing locally the onset of slippage at a model multicontact interface. *Phys. Rev. Lett.*, 112(9):094301, 2014. URL http://link.aps.org/doi/10.1103/PhysRevLett.112.094301.

[73] A. J. Rosakis, O. Samudrala, and D. Coker. Cracks faster than the shear wave speed. *Science*, 284(5418):1337–1340, 1999. URL http://www.sciencemag.org/content/284/5418/1337.abstract.

[74] S. Rubinstein, G. Cohen, and J. Fineberg. Detachment fronts and the onset of dynamic friction. *Nature*, 430(7003):1005–1009, 2004. URL http://dx.doi.org/10.1038/nature02830.

[75] S. M. Rubinstein, M. Shay, G. Cohen, and J. Fineberg. Crack-like processes governing the onset of frictional slip. *Int. J. Fract.*, 140(1-4):201–212, 2006. URL http://dx.doi.org/10.1007/s10704-006-0049-8.

[76] S. M. Rubinstein, G. Cohen, and J. Fineberg. Dynamics of precursors to frictional sliding. *Phys. Rev. Lett.*, 98(22):226103, 2007. URL http://link.aps.org/doi/10.1103/PhysRevLett.98.226103.

[77] S. M. Rubinstein, G. Cohen, and J. Fineberg. Visualizing stick-slip: experimental observations of processes governing the nucleation of frictional sliding. *J. Phys. D.: Appl. Phys.*, 42(21):214016, 2009. URL http://dx.doi.org/10.1088/0022-3727/42/21/214016.

[78] A. Ruina. Slip instability and state variable friction laws. *J. Geophys. Res.*, 88(B12):10359–10370, 1983. URL http://doi.wiley.com/10.1029/JB088iB12p10359.

[79] C. H. Scholz. *The Mechanics of Earthquakes and Faulting*. Cambridge University Press, Cambridge, second edition, 2002.

[80] I. Svetlizky and J. Fineberg. Classical shear cracks drive the onset of dry frictional motion. *Nature*, 509(7499):205–208, 2014. URL http://dx.doi.org/10.1038/nature13202.

[81] J. Trømborg, J. Scheibert, D. S. Amundsen, K. Thøgersen, and A. Malthe-Sørenssen. Transition from static to kinetic friction: Insights from a 2D model. *Phys. Rev. Lett.*, 107(7):074301, 2011. URL http://link.aps.org/doi/10.1103/PhysRevLett.107.074301.

[82] A. Vanossi, N. Manini, M. Urbakh, S. Zapperi, and E. Tosatti. Colloquium: Modeling friction: From nanoscale to mesoscale. *Rev. Mod. Phys.*, 85:529–552, 2013. URL http://link.aps.org/doi/10.1103/RevModPhys.85.529.

[83] K. W. Xia, A. J. Rosakis, and H. Kanamori. Laboratory earthquakes: the sub-Rayleigh-to-supershear rupture transition. *Science*, 303(5665):1859–1861, 2004. URL http://dx.doi.org/10.1126/science.1094022.

[84] Z. Yang, H. P. Zhang, and M. Marder. Dynamics of static friction between steel and silicon. *Proc. Natl. Acad. Sci. U. S. A.*, 105(36):13264–13268, 2008. URL http://www.pnas.org/content/105/36/13264.abstract.

[85] H. Yim and Y. Sohn. Numerical simulation and visualization of elastic waves using mass-spring lattice model. *IEEE T. Ultrason. Ferr.*, 47(3):549–558, 2000. URL http://dx.doi.org/10.1109/58.842041.

[86] M. D. Zoback, A. Kohli, I. Das, and M. McClure. The importance of slow slip on faults during hydraulic fracturing stimulation of shale gas reservoirs. In *SPE Americas Unconventional Resources Conference*, page 155476, 2012. URL http://dx.doi.org/10.2118/155476-MS.

APPENDIX A

Arguments for using the velocity Verlet / leapfrog integration scheme

In this appendix I provide the rationale behind my choice of numerical integration scheme. The properties of the velocity Verlet / leapfrog scheme are usually derived for systems where the forces only depend on the positions of the masses, and not on their velocities. In my simulations there is damping that depends on the relative velocity of blocks. I show here (by example) that this reduces the method to first order, but argue that it remains a good choice of integrator.

A.1 Properties of numerical integration schemes

For many problems in physics, including our spring–block model, the equations of motion are a set of coupled ordinary differential equations. In abstract form they read

$$\frac{\mathrm{d}\mathbf{x}_i}{\mathrm{d}t} = \mathbf{v}_i, \tag{A.1}$$

$$\frac{\mathrm{d}\mathbf{v}_i}{\mathrm{d}t} = \frac{\mathbf{F}_i}{m_i}, \tag{A.2}$$

where $\mathbf{x}_i$ is the position of block i, $\mathbf{v}_i$ is the velocity of the block, $\mathbf{F}_i$ is the net force on the block and m_i is the mass of the block. The interactions between the blocks, and between the blocks and the boundaries, including friction, are included in the net force $\mathbf{F}_i$. Because the forces on block i depend on the positions and velocities of its neighbouring blocks, the equations are coupled. To solve the equations numerically the derivatives are replaced by approximations which turn the equations from differential equations into difference equations. Different approximations have different properties and while some are poor and can be ruled out, which one is best depends both on what you think is important and on the properties of the equations of motion, which are in turn determined by the interactions that give rise to the forces.

Fundamentally, all time integration schemes perform the following task: from the state in the past and present, find the state in the future. To be more specific, the task is to calculate the state at time $t + \Delta t$ when the state at t, and possibly at earlier times, is known. By going forward in (usually small) steps Δt, the state at some start time t_0 can be evolved to find the state at some much later time t_1. The quality of

the results is judged by how closely the numerical solution resembles the analytical solution of the differential equations. One useful categorization of integration schemes distinguishes between

1. low-order integrators that use many small time steps Δt, where each step is computationally cheap,

2. higher-order integrators that exploit the smoothness of the solution to take longer (often adaptive) time steps Δt, at increased computational cost of each step.

Among the higher-order integrators a useful further grouping is into

2a. integrators that make trial steps that are temporary and are discarded each time a full step is taken,

2b. integrators that use a series of sub-steps and then extrapolate from these to a longer full step,

2c. integrators that store information of the previous states in addition to the current state.

Runge–Kutta integrators are a well-known example of type 2a. The Bulirsch–Stoer method is of type 2b. The terms multistep/multivalue are used for type 2c, which includes the Adams–Bashforth–Moulton schemes. Hybrid approaches that combine two of these strategies are also possible.

It is clear that for higher-order methods to outperform low-order methods the additional cost of each step must be more than offset by the ability to take longer steps. An example serves to make this clear. The computationally heavy part is usually the force evaluation, and the Runge–Kutta method of fourth order (RK4) uses four force evaluations per full time step. The leapfrog method, a low-order method, uses a single force evaluation per full time step. RK4 outperforms leapfrog only if the same accuracy can be achieved with a time step more than four times larger than the time step used in the leapfrog integration.

Although I have no stringent proof, it is my belief that two aspects of my spring–block simulations favour simple, low-order methods:

1. the friction force laws have discontinuities,

2. the maximal time step length is limited not by accuracy, but by the need to resolve the oscillatory motion of the blocks, that is, stability.

That the force discontinuities, which make the solution non-smooth, effectively rule integrators of type 2b and 2c out, is supported by Press et al. [66, Chap. 17.3 and 17.6]. This is because the advantage of the methods, namely the ability to take very long steps, is lost when it is necessary to tip-toe carefully across the discontinuities. Adaptive stepsize Runge–Kutta methods can handle discontinuities well, but I will argue below that the need to resolve the oscillatory motion means that the extra cost of each step compared to the leapfrog method is not recovered by taking longer steps.

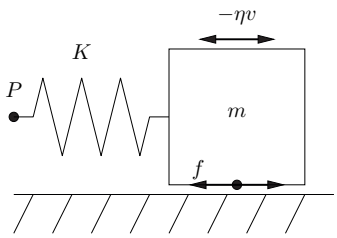

Figure A.1: A sliding system consisting of a single block and a driving spring. K is the spring stiffness, m is the slider mass, v is the slider velocity and f represents Amontons–Coulomb friction. The double-headed arrows indicate friction and damping acting against the direction of block motion. The force in the spring is increased by moving the point P slowly.

A.2 Example problems: harmonic oscillator with and without friction

Two example problems will serve to make the discussion more hands-on. They are not attempts at proving that *all* higher-order methods run into the same problems, and should be seen rather as illustrations of how discontinuities can affect the quality of the numerical solutions. I also do not claim that the leapfrog method is *the best* integrator that can be found for the problem at hand, but merely that it is a reasonable choice.

Consider the system in Figure A.1. If the surface is frictionless the system is a damped harmonic oscillator, which has a smooth solution. If Amontons–Coulomb friction acts at the interface the net force is discontinuous at the instant when the static friction threshold is overcome, and the solution is non-smooth. I use Amontons–Coulomb friction as an example, because it allows me to compare the numerical results to an exact analytical solution, but I expect the discontinuities in the friction law I have used in the publications to present the same difficulty for the integrators.

Figure A.2a shows the harmonic oscillator in the frictionless, underdamped case. Because the analytical solution is known, the order of the leading error term in the numerical solutions of the same problem can be found by varying the timestep and comparing the results. Figure A.2b shows the global error in position, which I have measured as $\epsilon = \text{mean}(|x_{\text{num}}(t) - x_{\text{an}}(t)|)$, with x_{num} and x_{an} the numerical and analytical solutions, respectively. As expected, Beeman's method[1] is of order $O(\Delta t^3)$ while the second order Runge–Kutta method is $O(\Delta t^2)$. The leapfrog method is $O(\Delta t)$. Note that when there is no velocity dependence in the force, which in this system requires

[1] A variant of Beeman's method for systems where the forces depend on both positions and velocities is http://en.wikipedia.org/wiki/Beeman's_algorithm [Accessed 2013-12-16]

$$x(t+\Delta t) = x(t) + v(t)\Delta t + \frac{1}{6}\left(4a(t) - a(t-\Delta t)\right)\Delta t^2 + O(\Delta t^4) \tag{A.3}$$

$$v_{\text{predicted}}(t+\Delta t) = v(t) + \frac{1}{2}\left(3a(t) - a(t-\Delta t)\right)\Delta t + O(\Delta t^3) \tag{A.4}$$

$$a(t+\Delta t) = \frac{1}{m}F\big(x(t+\Delta t), v_{\text{predicted}}(t+\Delta t)\big) \tag{A.5}$$

$$v_{\text{corrected}}(t+\Delta t) = v(t) + \frac{1}{12}\left(5a(t+\Delta t) + 8a(t) - a(t-\Delta t)\right)\Delta t + O(\Delta t^3) \tag{A.6}$$

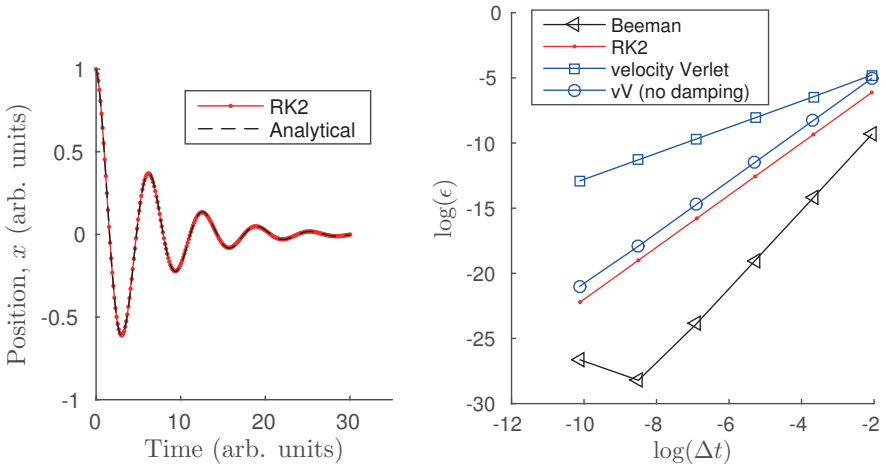

(a) Time evolution of block position. **(b)** Global numerical error in position.

Figure A.2: Numerical integration of the motion of a damped harmonic oscillator. The slopes of the error lines are 1, 2 and 3. For the smallest timesteps used with the Beeman method the error starts increasing again as round-off error in the computation starts dominating the truncation error of the method. The velocity Verlet (vV) results for the un-damped problem were included to demonstrate the expected $O(\Delta t^2)$ scaling of this method when the forces depend only on positions and not on velocities.

that the damping is turned off, the leapfrog method is $O(\Delta t^2)$ as expected.

Contrast the results in Figure A.2 with those in Figure A.3, which differs only in that Amontons–Coulomb friction acts at the interface. The block starts at rest and remains at rest as long as the force in the spring remains below the static friction threshold. Increasing the force slowly by moving the left end of the spring eventually triggers the motion of the block, and from then on the driving point is stopped in place. The block moves to the right. After one quarter of a full oscillation the block comes to rest and since the force in the spring is now lower than the static threshold, the block is stuck again. Figure A.3b shows that the integrators, which differed in their order of accuracy in the frictionless case, now all have the same $O(\Delta t)$ accuracy.

A.3 Time step is limited by need to resolve oscillations

There are at least three considerations that combine to determine the appropriate timestep length. The first is stability. Solution of wave problems with explicit integrators (the equations of elasticity admit waves and the methods I consider here are explicit) is stable only if the timestep is smaller than some threshold value. If a timestep larger than the threshold is chosen, the numerical scheme will pick up spurious terms that quickly grow to infinity and ruin the solution. The stability threshold is a function of the spatial discretization; the exact solution is known for some schemes [53], but in this work I have settled for verifying the stability of the solution in the

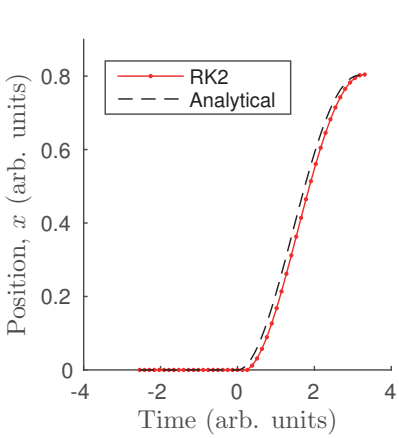

(a) Time evolution of block position. In the analytical solution the onset of sliding occurs at $t = 0$.

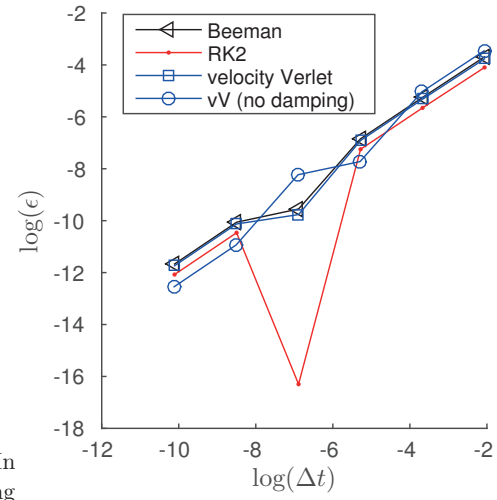

(b) Global numerical error in position.

Figure A.3: Numerical integration of the motion of a spring–block system under Amontons–Coulomb friction. The common slope of the error lines is 1. The smaller error at $\Delta t \approx 10^{-7}$ is due to a fortuitous matching of the discrete values of the time step and the true value of the moment of sliding initiation and cannot be relied upon in a real simulation. The sliding onset is triggered by moving the point P (see Figure A.1) on the spring until the static friction threshold is reached; then the driving point is stopped in place. The magnitude of the error depends on the driving velocity, but the scaling result does not.

post-run analysis.

The second consideration is wall clock time, which favours larger time steps. A set of physical parameters determines the total system time $t_{\text{stop}} - t_{\text{start}}$ required to observe whatever is interesting. For larger Δt this interval is traversed in fewer timesteps, and because the computational cost of each time step is independent of Δt, fewer timesteps translates to shorter wall clock time. The simulations I have performed have typically taken from an hour to half a day with my code and on the hardware available. This means that the number of ideas that can be tested depends on the timestep. There is a large difference in how well ideas are generated depending on whether questions can be answered the same day or the day after, or in a few days or a week.

The third consideration is accuracy. This usually favours small timesteps, as is shown in both Figures A.2 and A.3. However, this is not always the case. For the simple wave equation without damping it can be shown that the best accuracy is achieved *at* the stability threshold [53, Appendix A.4]. Since I have not performed an exact stability analysis I do not know if this remains true with friction as a boundary condition.

In the end I have chosen a timestep that strikes a balance between wall clock time and accuracy. As consecutive blocks in the 1+1D system start sliding and, after some displacement, trigger the sliding of their neighbours, it is necessary to resolve their motion in time. Figure A.3a shows the resolution when the timestep is $T/50$ with T

the period of oscillation in the un-damped system of spring and block. It is clear that in a full system of blocks, if this block triggers the motion of its neighbour somewhere during this displacement, a resolution much poorer than this will be insufficient. On the other hand, a much smaller resolution means more timesteps, and a wall clock time longer than I have deemed satisfactory. Consequently, I have used a timestep of $\Delta t = T/50$. The fact that each block is connected to many others via springs of different stiffness only changes the period by a factor of order unity, so I have used $T = 2\pi/\omega$ with $\omega = \sqrt{k_{\text{horizontal,vertical}}/m}$, where $k_{\text{horizontal,vertical}}$ is the stiffness of the springs connecting nearest-neighbour blocks.

A.4 Some comments

The leapfrog method is known by different names in different disciplines. It is equivalent to the velocity Verlet method save that velocity Verlet is commonly written with the velocity update performed in two steps so that the velocities are known at the same instants as the positions.

The velocity Verlet method is a *symplectic* integrator, which means that it does not have long-term drift in the energy of the system. For applications like celestial mechanics and molecular dynamics this can be of paramount importance. In fact, the combination of being symplectic, second order global accuracy (when the forces do not depend on velocities), a single force evaluation per full time step and low memory overhead is hard to beat in these cases. In my friction simulations, however, the energy in the problem is not conserved: the driving continually adds energy, while friction and bulk dissipation let energy leave the system. Therefore, choosing an integrator that conserves energy is not a necessity. However, lifting this requirement does not detract from the strength of the other arguments for using the leapfrog method.

APPENDIX B

Bulk wave speed equations and code verification

In this chapter I review the relationship between the spring–block parameters of the bulk model, the elastic moduli that they represent and the corresponding bulk wave speeds. I also provide verification of my spring–block code by measuring the bulk wave speeds in simulations performed without friction.

B.1 2D elastic wave equations

The longitudinal (P) and shear (S) wave speeds in a linear, isotropic elastic medium depend on the mass density ρ and the elastic constants of the medium. They are

$$c_p = \sqrt{\frac{\lambda + 2\mu}{\rho}}, \tag{B.1}$$

$$c_s = \sqrt{\frac{\mu}{\rho}}, \tag{B.2}$$

where λ and μ are the Lamé parameters. In 3D the Lamé parameters are related to the Young modulus and Poisson ratio of the medium as

$$E = \frac{\mu(3\lambda + 2\mu)}{\lambda + \mu}, \tag{B.3}$$

$$\nu = \frac{\lambda}{2(\lambda + \mu)}. \tag{B.4}$$

In a 2D representation the choice of plane strain or plane stress conditions does not affect the form of the elasticity equations; instead, the relationships between the sets of elastic constants are different in plane strain and plane stress. The stress–strain

relationships in 2D are given by Landau and Lifshitz [52, Equations 3.12 and 5.13]:

Plane stress:

$$\begin{bmatrix}\sigma_{xx}\\ \sigma_{yy}\\ \sigma_{xy}\end{bmatrix} = \frac{E_\sigma}{1-\nu_\sigma^2}\begin{bmatrix}1 & \nu_\sigma & 0\\ \nu_\sigma & 1 & 0\\ 0 & 0 & \frac{1-\nu_\sigma}{2}\end{bmatrix}\begin{bmatrix}\varepsilon_{xx}\\ \varepsilon_{yy}\\ 2\varepsilon_{xy}\end{bmatrix}, \tag{B.5}$$

Plane strain:

$$\begin{bmatrix}\sigma_{xx}\\ \sigma_{yy}\\ \sigma_{xy}\end{bmatrix} = \frac{E_\varepsilon}{(1+\nu_\varepsilon)(1-2\nu_\varepsilon)}\begin{bmatrix}1-\nu_\varepsilon & \nu_\varepsilon & 0\\ \nu_\varepsilon & 1-\nu_\varepsilon & 0\\ 0 & 0 & \frac{1}{2}(1-2\nu_\varepsilon)\end{bmatrix}\begin{bmatrix}\varepsilon_{xx}\\ \varepsilon_{yy}\\ 2\varepsilon_{xy}\end{bmatrix}. \tag{B.6}$$

Here the subscripts in E_σ and ν_σ denote that these are plane stress values, and the subscripts in E_ε and ν_ε denote plane strain. One can show by insertion in these equations that plane strain with parameters $(E_\varepsilon, \nu_\varepsilon)$ is mathematically equivalent to plane stress with

$$E_\sigma = \frac{E_\varepsilon}{1-\nu_\varepsilon^2}, \tag{B.7}$$

$$\nu_\sigma = \frac{\nu_\varepsilon}{1-\nu_\varepsilon}. \tag{B.8}$$

The plane strain relationships between the Lamé parameters and the Young modulus and Poisson ratio are [57]

$$E_\varepsilon = \frac{4\mu(\lambda+\mu)}{\lambda+2\mu}, \tag{B.9}$$

$$\nu_\varepsilon = \frac{\lambda}{\lambda+2\mu}, \tag{B.10}$$

which differ from their 3D counterparts in equations (B.3) and (B.4).

With $\mathbf{u}$ the displacement field, the elastic wave equation is

$$\rho\frac{\partial^2\mathbf{u}}{\partial t^2} = \lambda\nabla(\nabla\cdot\mathbf{u}) + \mu\nabla(\nabla\cdot\mathbf{u}) + \mu\nabla^2\mathbf{u}. \tag{B.11}$$

Plane strain conditions amount to setting $u_z = 0$, $\frac{\partial u_x}{\partial z} = \frac{\partial u_y}{\partial z} = 0$, that is, no motion and no variation along the z axis. You can show by linearising our spring–block model that it corresponds to a discretization of the elastic wave equation under plane strain conditions [57, 85]. The relationships between the parameters are

$$\lambda = \mu = k/2, \tag{B.12}$$

$$k = k_1 = 2k_2. \tag{B.13}$$

Note that there is a convention difference here between my notation and that in [57, 85]: I have let k denote the stiffness k_1 of the nearest-neighbour springs in the lattice, while they have used k for the stiffness k_2 of the next-nearest-neighbour springs.

It follows from equations (B.9), (B.10) and (B.12) that $E = 4k/3$, $\nu = 1/3$. An additional parameter is required to adjust ν [57, 85]. In order to make use of the 3D experimental values of E and the mass density ρ I have additionally included the width B of the slider (in the y-dimension, which is left out of the 2D equations). Because E has dimension force per area, k has dimension force per length, and ρ has dimension mass per volume, including B gives $k = \frac{3BE}{4}$ and slider mass $M = \rho LBH$, where L is the length and H is the height of the slider.

B.2 Verification of the bulk spring–block implementation

To verify the mapping from bulk moduli to model parameters and the implementation of the bulk part of the model I have measured the bulk wave speeds in the model and compared them to equations (B.1) and (B.2). To measure the bulk wave speeds in the model I have set up simulations with a different set of boundary conditions from what I use in the friction simulations.

A longitudinal wave in the x-direction can be set up as follows:

- To the undeformed lattice, add a displacement field in the x components only. I have used the functional form $u_x = \frac{L_x}{10^4} e^{-\frac{(x-L_x/2)^2}{2(L_x/20)^2}}$.
- Boundary conditions on the left- and righthand sides do not matter except to the phase of the reflected waves, but in order to avoid generating secondary waves at the top and bottom it is important to impose $u_z = 0$ while letting u_x be free (zero traction).
- Let all velocities $\mathbf{v} = 0$ initially. Then solve the equations of motion of the blocks forwards in time.

A shear wave in the x-direction is set up in the same manner, but adding the initial displacement to u_z, and keeping $u_x = 0$, u_z free on the top and bottom surfaces. Snapshots of a longitudinal and a shear wave from two simulations are shown in Figure B.1.

From the wave propagation I have measured the time ΔT_{wave} it takes the maxima in the displacement field to travel across the sample. The wave speed is then

$$v_{\text{wave}} = \frac{\Delta T_{\text{wave}}}{L_x}.$$

The results are shown in Table B.1. Figure B.2 shows that extrapolating to the limit of $\Delta x = \Delta t = 0$ gives good agreement with the analytical results. In Table B.1 the Δx and Δt are varied independently, and so their ratio varies between the simulations. While it is common to use the Courant number[1] to determine the optimal Δt, I have instead taken the time step used in my simulations with friction as the reference point. This time step was discussed in Section A.3. The results in Table B.1 show very little variation in wave speed when Δt is reduced and Δx is held fixed. Note also that I find approximately the same wave speeds for $\eta_r = 0$, $\sqrt{0.1}$, 0.5, i.e. the bulk wave speeds are independent of the damping coefficient. Contrast this with the rupture front speed, which in Publication 4 (1D) was found to depend on the damping coefficient. Preliminary results indicate that the same dependency of rupture front speed on damping coefficient holds in 2D.

Finally, note that the sound speeds reported by the group of Fineberg [11, 75, 80] are higher than the sound speeds I calculate here, even though I have used the mass

[1] The Courant number is a standard tool in the analysis of numerical methods, see for example [53, 66]. It can be interpreted as the ratio of the characteristic speed of the physical problem to the "characteristic speed" $\Delta x/\Delta t$ of the numerical scheme, with prefactors that depend on the details of the numerical scheme. Instabilities arise if the Courant number is larger than unity, see Press et al. [66, Figure 20.1.3] for a graphical interpretation. For simple wave problems the highest accuracy is achieved at the stability limit, making this the optimal choice of Δt for a given Δx.

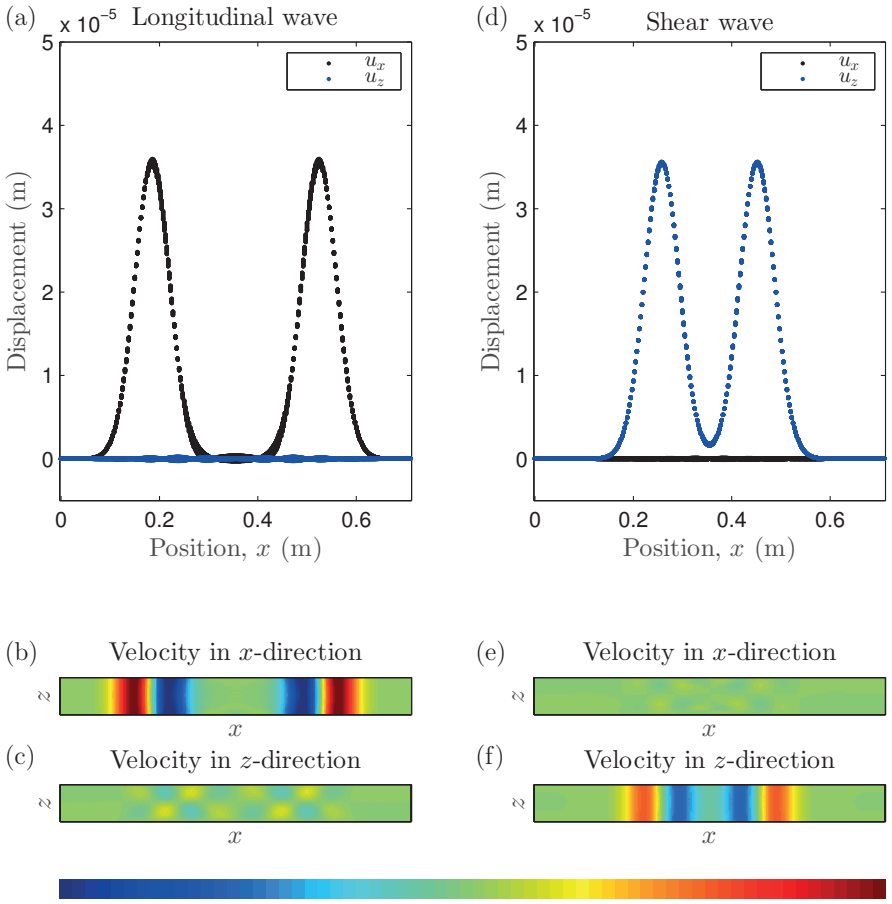

Figure B.1: Simulations to measure bulk wave speeds. Left column: a longitudinal wave. Right column: a shear wave. Data corresponds to $\Delta x = \Delta z = 2.5$ mm, $\Delta t = 2 \cdot 10^{-7}$ s, $\eta_r = 0$ in Table B.1 taken at time $t = 0.1$ ms. The initial displacement fields are constant in the z-direction, so in panels (a) and (d), values for equal z plot (nearly) on top of each other. The colorscale range for panels (b) and (f) is $[-1, 1]$ m/s; for panels (c) and (e) the range is $[-0.1, 0.1]$ m/s, to better exhibit the variations. In the analytical solution of the wave equation with these initial and boundary conditions, the v_z components in (c) and the v_x components in (e) are exactly zero. Their amplitude in the numerical solution could be used as a measure of the numerical error; I have instead investigated the deviation in the sound speeds from their values in Equations (B.1) and (B.2), see Figure B.2.

Table B.1: Bulk wave speed measurements for simulations in which there is no friction nor normal load, the top and bottom boundary conditions are fixed+free to support either P or S waves along x, and a bulk wave is initiated by imposing an exponential, vertically symmetric displacement field at $t = 0$. With $E = 3$ GPa, $\nu = 1/3$ and $\rho = 1200$ kg/m^3, $c_p = 1677$ m/s and $c_s = 968$ m/s. The internal viscous damping parameter η_r is defined in Publication 1 (all the simulations in this table are underdamped).

$\Delta x = \Delta z$ (mm)	Δt (ns)	η_r	c_p (m/s)	c_s (m/s)
5	200	0	1702.9	961.6
2.5	200	0	1691.3	965.7
1.25	200	0	1684.5	967.2
0.625	200	0	1680.9	967.8
0.3125	200	0	unstable	unstable
5	200	$\sqrt{0.1}$	1704.3	961.7
2.5	200	$\sqrt{0.1}$	1691.4	965.3
1.25	200	$\sqrt{0.1}$	1684.5	967.0
2.5	100	$\sqrt{0.1}$	1691.2	965.2
2.5	50	$\sqrt{0.1}$	1691.1	965.2
2.5	25	$\sqrt{0.1}$	1691.1	965.2
1.25	200	0.5	1684.3	966.6

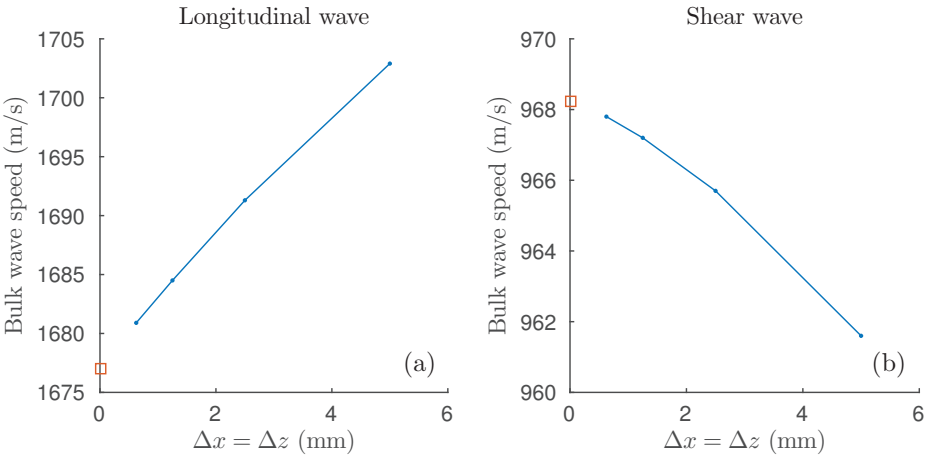

Figure B.2: The bulk wave speeds in the simulations converge to their values in Equations (B.1) and (B.2) with increasing spatial resolution. The lines show the $\Delta t = 2 \cdot 10^{-7}$ s, $\eta_r = 0$ data in Table B.1, the squares on the vertical axes show the analytical results. I have used this simple study only to verify my implementation of the spring–block model. For an in-depth analysis of the wave propagation properties of spring–block models, see e.g. Yim and Sohn [85].

density and Young modulus that they report. This is because the Young modulus is time-scale dependent. Elastic waves sample the short time-scale modulus. Static deformation samples the long time-scale modulus. This point is discussed in more detail in [68], see also [80, Methods].

APPENDIX C

Selected modelling results that do not appear in the publications

C.1 The front speed evolution in a partial slip event

In Publications 1 and 3 we presented spatiotemporal plots of the fraction of attached junctions. These are the counterpart within the model to experimental figures showing the spatiotemporal evolution of the light transmitted through the interface, which is proportional to the real area of contact. In our publications, we only showed the data from full sliding events, to highlight the distinction between fast-only and fast-slow-fast events. Figure C.1 shows example data from a partial slip event, to illustrate that this too closely resembles the experimental results. For ease of comparison I have also included the experimental results.

C.2 The slow-fast transition occurs where the previous partial slip event arrested

In Publications 1 and 3 we discussed the transition from fast to slow rupture propagation in fast-slow-fast events. The transition back to fast rupture, when it happens, we understand less well. It can happen both in interfaces with a heterogeneous stress and strength state and in interfaces with a homogeneous stress and strength state.

In the full simulation of Publication 1, where a sequence of events is produced by driving the system from the side, the stick–slip cycle alternates between partial slip events and full sliding events. For the fast-only events there is no slow-fast transition, of course, but for Events I and II, which are of the fast-slow-fast type, a slow-fast transition occurs. Figure C.2 shows that this slow-fast transition occurs at the arrest point of the preceding partial slip event. We believe that this is due to the higher level of shear stress stored near the arrest point. As is shown in Publication 3, higher shear prestress favours faster front propagation, and can bring an event from the slow into the fast regime.

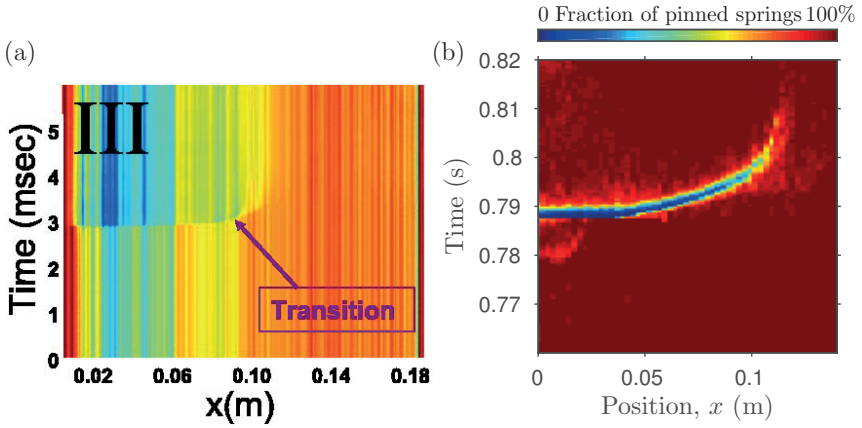

Figure C.1: Partial slip events can also exhibit the fast-slow transition. (a) Experimental result from Rubinstein et al. [76]. Real area of contact $A(x,t)$ normalized against $A(x)$ at zero driving force. (b) Simulation result from the same simulation as in Fig. 1D and Fig. 2 of Publication 1. The experimental result is for a precursor. The simulation result is for a partial slip event during the stick–slip cycle, chosen for showing the fast-slow transition clearly. In the model, the mechanism behind the fast-slow transition for partial slip events is the arrest of the fast rupture and the subsequent slow slip motion behind the front tip, as explained in Publication 1. Panel (a) reprinted with permission from [76]. Copyright 2007 by the American Physical Society.

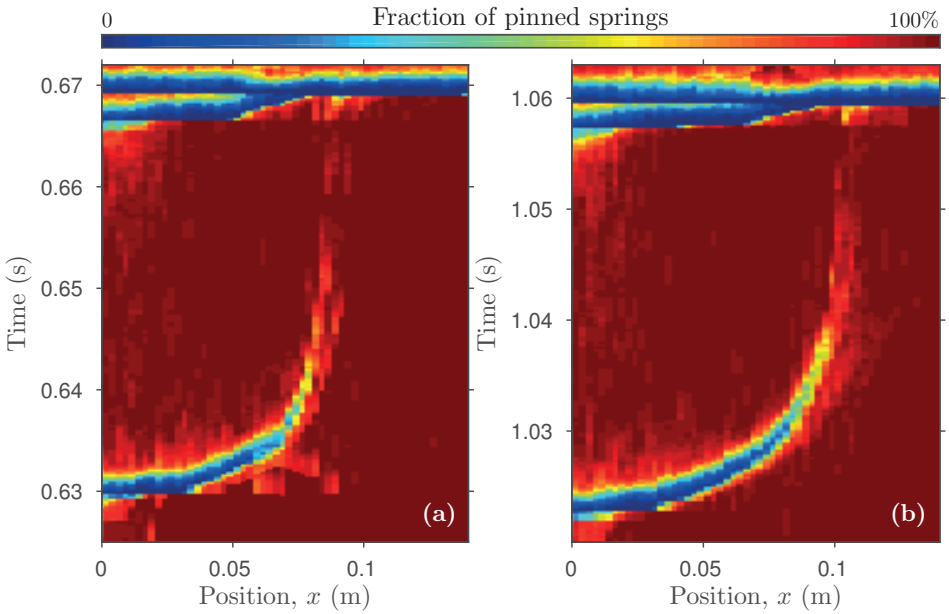

Figure C.2: In Events I and II from Publication 1, the slow-fast transitions occur at the arrest point of the preceding partial slip events. The events can be identified by the time at which they occur.